Reduced chemical reaction mechanisms for simulating sodium emissions by solid-fuel combustion

Kaidi Wan [a,b,c], Luc Vervisch [c], Zhenxun Gao [a,b,*], Pascale Domingo [c], Chongwen Jiang [a,b], Zhihua Wang [d], Jun Xia [e], Yingzu Liu [d], Kefa Cen [d]

[a] *Aircraft and Propulsion Laboratory, Ningbo Institute of Technology, Beihang University, Ningbo 315832, China*
[b] *National Laboratory for Computational Fluid Dynamics, School of Aeronautic Science and Engineering, Beihang University, Beijing 100191, China*
[c] *CORIA – CNRS, Normandie Université, INSA de Rouen, 76801 Saint-Etienne-du-Rouvray, France*
[d] *State Key Laboratory of Clean Energy Utilization, Zhejiang University, Hangzhou 310027, China*
[e] *Department of Mechanical and Aerospace Engineering & Institute of Energy Futures, Brunel University London, Uxbridge UB8 3PH, UK*

ARTICLE INFO

ABSTRACT

Starting from a reference and comprehensive chemical mechanism for alkali metal emissions (Glarborg and Marshall, 2005), combined with an hydrocarbon oxidation described with a skeleton mechanism (Kazakov and Frenklach, 1994), reduced and optimized chemical kinetics are derived. The objective is to provide a set of chemical schemes useful for three-dimensional (3D) numerical simulations of alkali metal emissions by pulverized solid-fuel combustion systems. An automated procedure relying on one-dimensional (1D) premixed flames is applied to obtain a combined reduced mechanism, whose performance is then evaluated in one-dimensional strained diffusion flames, micro-mixing based canonical problems and three-dimensional carrier-phase direct numerical simulation (DNS) of coal combustion. Predictions of the reduced mechanism on major sodium species, i.e., Na, NaOH, NaCl and Na_2SO_4 agree well with that of the detail reference scheme under all the considered conditions. A parametric study with 14 two-dimensional (2D) DNS cases is then performed to better understand the reactive flow properties and estimate the prediction capabilities of the reduced mechanism for various Na/Cl/S ratio in the volatiles. After pursuing the chemistry reduction, a global sodium mechanism with only 9 species and 8 reaction-steps is also discussed. The systematic comparison between the 3D DNS results obtained with the reference chemical scheme against those with the reduced ones confirm the validity of the reduction strategy. A reduction of up to 84% in computational cost is reached with the optimized global scheme, thus allowing for addressing real pulverized-coal combustion systems.

1. Introduction

Alkali-induced slagging is one of the most challenging technical issues when implementing pulverized solid-fuel combustion for electricity production. This is the case for sodium-rich coals such as those from North Dakota in the US, Loy Yang in Australia and Zhundong in China [1]. Similarly, biomass also contains a significant amount of potassium leading to identical concerns [2]. The released alkali vapor condenses on heat exchange surfaces, to form a primary sticky layer promoting massive ash deposition on walls [3,4]. Alkali also reacts with chlorine and sulfur, to produce complex compounds, which could result in the fouling and the corrosion of the heat exchange surfaces [5]. These alkali-induced problems jeopardize the clean and efficient use of potassium-rich biomass and sodium-rich coals and therefore recently

attract significant attention in the solid-fuel research community especially in China, see [6–15].

In the context of solid-fuel combustion, the knowledge on alkali emissions benefited from measurements evolving from offline sampling to time-resolved online laser diagnostics. van Eyk et al. [16,17] developed a quantitative planar laser-induced fluoresence (PLIF) technique to measure the release of atomic Na from a burning coal pellet, but failed to capture the sodium release during the coal pyrolysis stage due to the strong scattering by soot particles. Later on, He et al. [18] adapted a laser-induced breakdown spectroscopy (LIBS) technique to detect sodium during all stages of coal combustion, including the sooting pyrolysis stage. This was then extended to a multi-point LIBS approach by Liu et al. [19], to provide spatially resolved sodium measurements, while the scattering disturbance during the coal pyrolysis

stage was addressed by Wang et al. [20] through improved non-resonant PLIF. These multi-point LIBS and non-resonant PLIF techniques were also applied to biomass combustion for potassium measurements [21], to calibrate global one- or two-step alkali release chemical kinetics [19–22]. In these studies, the pellet diameter (about 4 mm) and burnout time are of the order of magnitude of those of a typical circulating fluidized bed (CFB) boiler [19] and therefore the developed alkali release kinetics cannot be directly implemented in pulverized-coal combustion (PCC).

Considering the post-release gaseous alkali chemistry, the final compositions of alkali in burnout gases is usually well captured from thermodynamic equilibrium [4,19,23], with the species Na, NaOH and NaCl and K, KOH and KCl [23]. The first detailed alkali chemical kinetics mechanisms were developed by Srinivasachar et al. [24] and Steinberg and Schofield [25]. Then, Glarborg and Marshall [26] proposed a detailed alkali mechanism encompassing the elements Na, K, C, H, O, S and Cl, with careful validation against experiments of homogeneous sulfatation of alkali chloride under combustion conditions [27]. With this detailed alkali mechanism, Takuwa and Naruse [28] investigated the behaviour of sodium compounds in hydrogen-air combustion.

The reference detailed alkali mechanism [26] includes 48 Na/K/O/H/Cl/S species and 202 elementary reactions. Such a complexity level restricts its application mostly to canonical problems. Thereby, in the literature the reported numerical studies of real combustion systems tackling alkali, employ simplified versions of this chemical scheme, e.g., a subset of the detailed mechanism. Akbar et al. [29] used a K/O/H/Cl subset with 14 reactions to analyze with Reynolds-Averaged Navier-Stokes (RANS) the potassium thermochemistry in a 0.5 MW pulverized-fuel combustion facility. Wan et al. [30] employed a Na/O/H subset with 24 reactions to investigate the dynamics of sodium emissions in an early-stage pulverized-coal flame using direct numerical simulation (DNS). In other computational fluid dynamic (CFD) studies, the reference detailed alkali mechanism was reduced to allow for complex geometry simulations. Along these lines, Garba et al. [31] developed a reduced mechanism including 36 K/O/H/Cl/S species and 137 reactions using sensitivity analysis and applied it to RANS of a 10 MW biomass-fired furnace. Kang and Ding [6] developed a reduced Na/O/H/Cl/S mechanism containing 32 elementary reactions also based on sensitivity analysis and the mechanism was used for RANS of a 660 MW PCC boiler burning Zhundong coal. Ji et al. [8,32] proposed a 6-step gaseous sodium mechanism and applied it to RANS of CFB furnaces. Nevertheless, to the best of our knowledge, a systematic reduction study of detailed alkali mechanisms has not been reported yet, reduction which could benefit to virtual prototyping of solid-fuel combustion systems.

Carrier-phase DNS [33–39] plays a more and more important role in exploring the underlying physics of PCC since its first use by Luo et al. [33]. In carrier-phase DNS, also called point-particle DNS [34], the solid-fuel particles are not resolved but tracked as point sources via the particle-source-in-cell (PSIC) model [40]. To ease the reading, 'carrier-phase DNS' is denoted as 'DNS' in the following. Muto et al. [35,36] investigated ignition and soot formation of PCC in a two-dimensional (2D) mixing layer using DNS with a detailed chemical mechanism involving 158 species and 1804 reactions for describing the gas-phase combustion. Hara el al. [37] developed a precise two-step global reaction scheme for gaseous volatile combustion, which is applicable to various coal types and is validated against the detailed 158-species mechanism. The two-step global scheme was then coupled with three-dimensional (3D) DNS to simulate a lab-scale pulverized-coal jet flame [37] and the validity of the DNS was confirmed by comparing the simulation results with those in previous measurements [41]. These state-of-the-art applications of DNS in PCC field confirm the merits of this numerical approach in exploring the specific reacting flow physics features of solid-fuel combustion [34].

Within this context and considering only one alkali metal, Na, the aim of the present study is threefold. First, for representative operating conditions, a reduced sodium skeletal mechanism is developed from the reference detailed one by Glarborg and Marshall [26], com-

Table 1
Representative volatile compostions of Loy Yang brown coal.

Hydrocarbon volatile compositions (mass fractions)					
CH_4	C_2H_2	CO	H_2	CO_2	H_2O
0.03707	0.30698	0.20664	0.02976	0.15394	0.25979
Non-hydrocarbon volatile compositions (mass fractions)					
NaOH	HCl	SO_2			
4.0E-4	6.2E-4	48.0E-4			

bined with the skeleton hydrocarbon oxidation mechanism by Kazakov and Frenklach [42]. Systematic reduction techniques and rate optimization [43,44] are combined to generate the reduced scheme. Second, the performance of this reduced mechanism is systematically examined in one-dimensional (1D) premixed flames, 1D diffusion flames, micro-mixing based canonical problems and 2D/3D DNS simulations. Third, a global sodium mechanism with only 9 species and 8 reactions is proposed, which could be of interest for design optimization requiring numerous simulations using most recent techniques, as digital twins [45]. The novelty of the present study lies in the fact that the reduced sodium mechanisms developed here help to bridge the gap between the computationally expensive detailed sodium chemistry and the CFD simulations of sodium emissions in practical solid-fuel furnaces.

2. Automated reduction and optimization of alkali metal chemical kinetics

According to previous DNS studies [30], because of strong partial premixing of the reactants after coal devolatilization, the sodium reactions are mostly occurring in a premixed-like combustion mode. The one-dimensional premixed flame configuration therefore serves as a reference problem to begin with the reduction of the reference mechanisms.

The volatile of Loy Yang brown coal [4] is employed, for which the coal properties are provided in supplementary material. The previously validated DRM22 mechanism proposed by Kazakov and Frenklach [42] is used to describe the hydrocarbon combustion of the volatile, which contains 22 chemical species and 104 elementary reactions. The compositions of the hydrocarbon volatile fuels are determined via the chemical percolation devolatilization (CPD) model [46,47], with the Tar species replaced by C_2H_2[48]. Representing tar by C_2H_2 is a crude approximation. Nevertheless, previous studies have shown that some of the major volatile combustion characteristics, such as ignition delay, are relatively insensitive to the representation of Tar by C_2H_2 [49]. This assumption can be considered valid unless soot formation needs to be accurately traced, then the choice of Tar species becomes critical. Besides, the choice of C_2H_2 is also motivated in this work by its availability in the DRM22 mechanism, selected for modeling the hydrocarbon oxidation part. As in previous works [50], minor adjustments have been applied to the compositions predicted by the CPD model to fulfil the elemental mass conservation. The final compositions are given in Table 1.

Following former studies [28], the initial sodium species in the volatile is set to be NaOH, while those of S and Cl are set to be SO_2 and HCl, respectively. Based on experimental measurements [4], it is assumed during coal pyrolysis that 19.1% of the mass of sodium present in the coal is released. No experimental information is however available for chlorine and sulfur. In this work, they are assumed to follow the ratio of volatile yields during pyrolysis as predicted by the CPD model, i.e., 55.1% of the mass of chlorine and sulfur is released with the volatiles. The content of NaOH, HCl and SO_2 in the volatile are then determined and given in Table 1.

The homogeneous reactions of Na/S/Cl species are simulated with the detailed mechanism by Glarborg and Marshall [26] containing the elements Na, K, C, H, O, S and Cl. Potassium is only weakly present
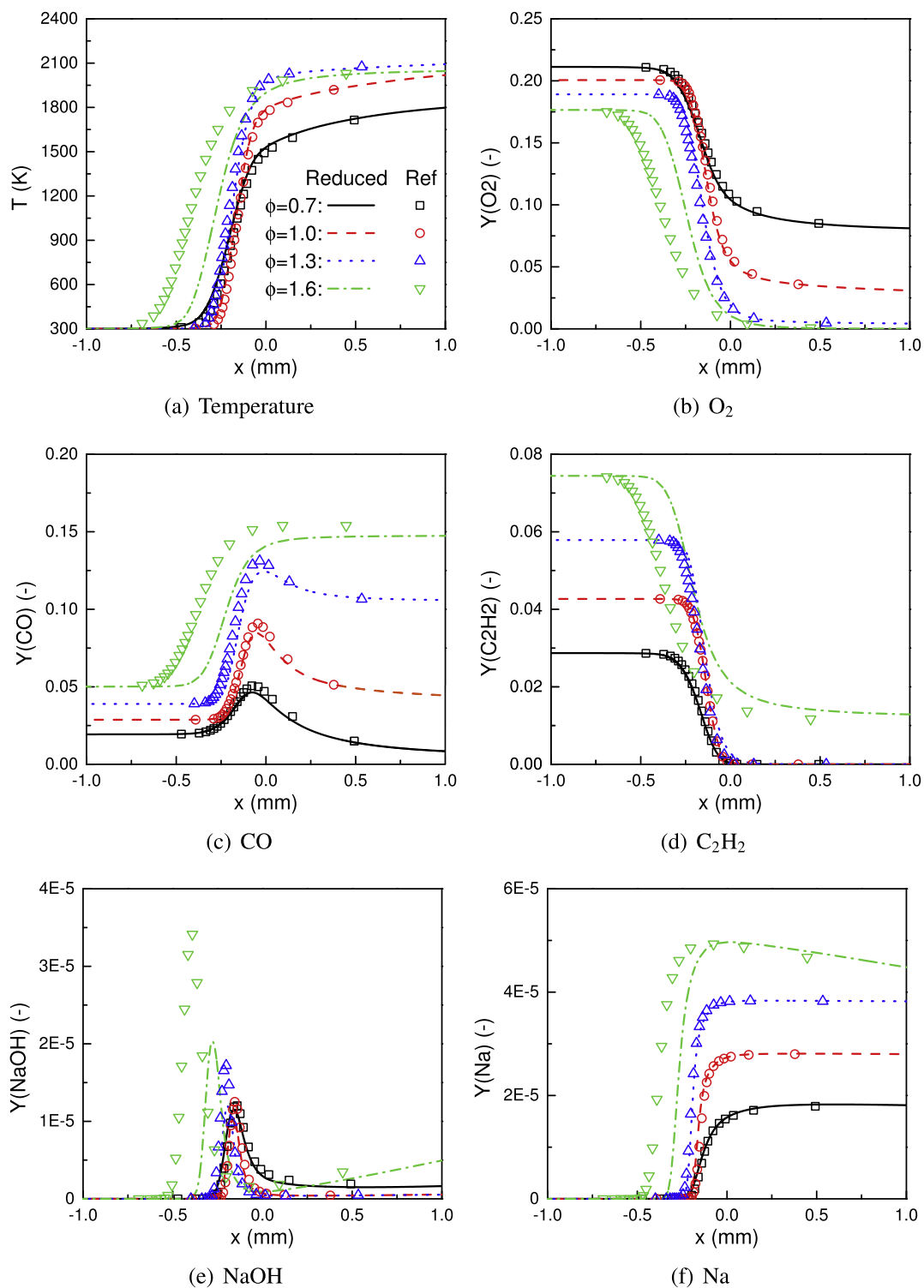
Fig. 1. Distribution of temperature and mass fractions in one-dimensional premixed flames. Black: Equivalence ratio $\phi = 0.7$. Red: 1.0. Blue: 1.3. Green: 1.6. Symbols: reference chemistry [26,42]. Lines: preliminary reduced mechanism (DRGEP, Table 2 but with original rates parameters). (For interpretation of the references to colour in this figure legend, the reader is referred to the web version of this article.)

in the coal considered (see supplementary material) and the element K is not considered, which leads to a reference detailed mechanism of sodium reactions involving 36 species and 153 elementary reactions.

The ORCh (Optimized and Reduced Chemistry) method, reported in detail in [43,44] and previously applied for modeling selective non-catalytic reduction [51] and meso-scale combustion [52], is coupled with the CANTERA [53] flame solver. In the present work, the targets for reduction and optimization are the distributions of thermochemical quantities through one-dimensional premixed flames. ORCh consists of a combination of directed relation graph with error propagation
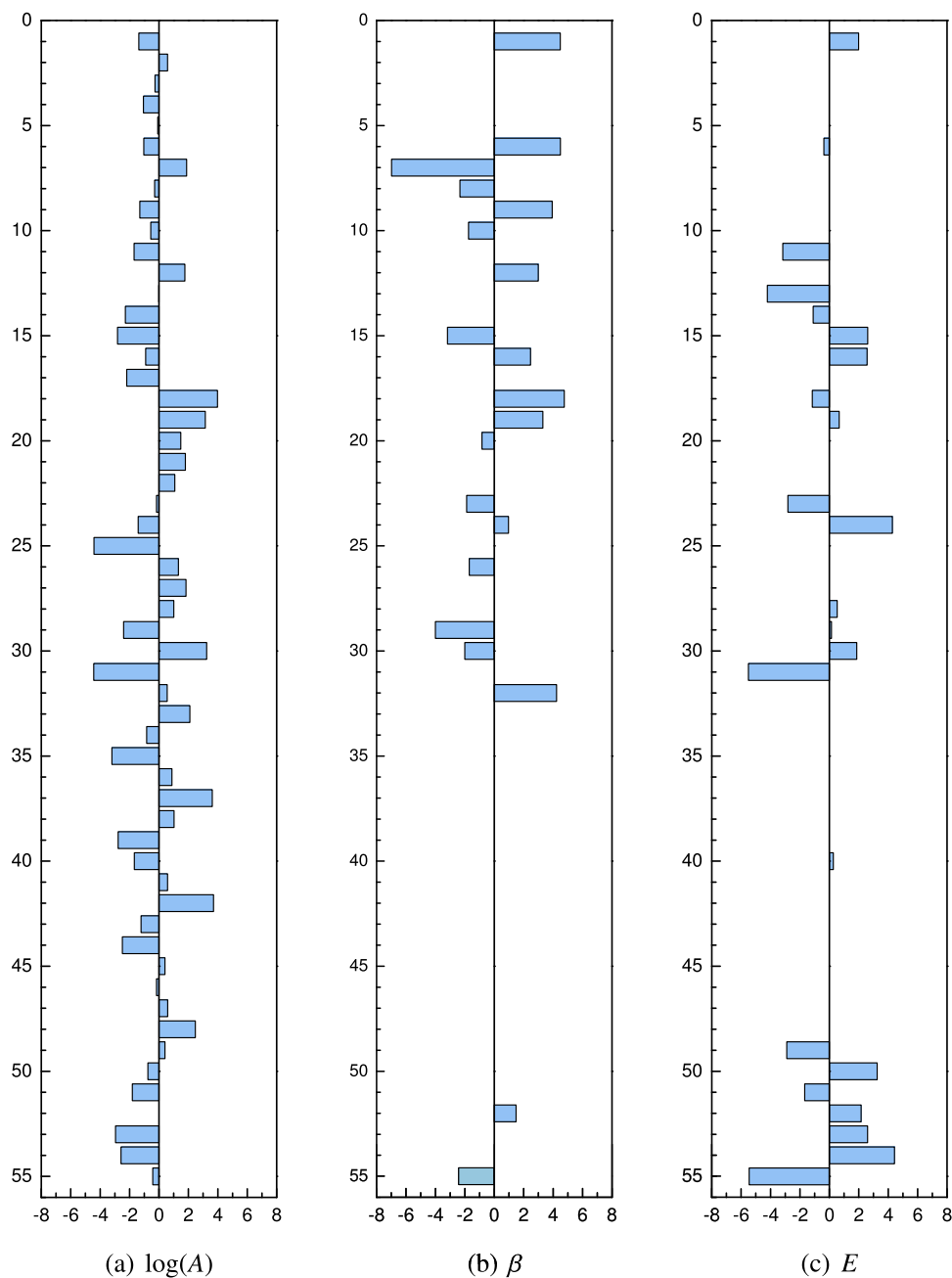
Fig. 2. Variation of the rate parameters of the reduced mechanism in % measured from the reference mechanisms [26,42]. Reactions are ordered as in Table 2.

(a) $\log(A)$

(b) β

(c) E

(DRGEP) [54,55] to remove the less influential reactions and species. To allow for reaching further reduced schemes, still reproducing most of the thermochemical properties, a genetic algorithm (GA) [56] is added to optimize the chemical rates of the reduced mechanism.

A set of target species is defined as the species which need to be accurately reproduced by the reduced mechanism. It includes the fuel CH_4, C_2H_2, CO and H_2, the oxidizer O_2, major combustion products CO_2 and H_2O, and major sodium species NaOH, Na, NaCl and Na_2SO_4.

During the DRGEP procedure (see [55] for detail), a set of reference one-dimensional flames are re-computed after sequentially removing radical species and elementary reactions. To proceed with this removal, species and reactions are automatically ordered according to their relative influence in the evolution of the set of target species listed above. This classification of the intermediate species is achieved by comparing the variation rate of a target species when an intermediate (non-target) species is involved against the total variation rate of that tar-

get species. From this information, the species are classified according to their relative importance in the evolution of a given target species [54,55].

2.1. Evaluation of the reduced mechanism in one-dimensional premixed flames

After removing species and reactions and recomputing the one-dimensional flames, the obtained distributions $\varphi_k(x_i; \phi^\ell)$ of the target species mass fractions and temperature are compared against $\varphi_k^{\text{Ref}}(x_i; \phi^\ell)$, their detailed chemistry responses. k denotes the kth targeted variables ($k = 1, \cdots, N_t = 12$, 11 species plus temperature), x_i is the ith mesh point ($i = 1, \cdots, N_x$) through the one-dimensional flame at equivalence ratio ϕ^ℓ. Four values of the equivalence ratio of the fresh mixture are simultaneously considered, one lean conditions, one stoichiometric and two rich mixtures ($\phi^1 = 0.7, \phi^2 = 1.0, \phi^3 = 1.3$ and
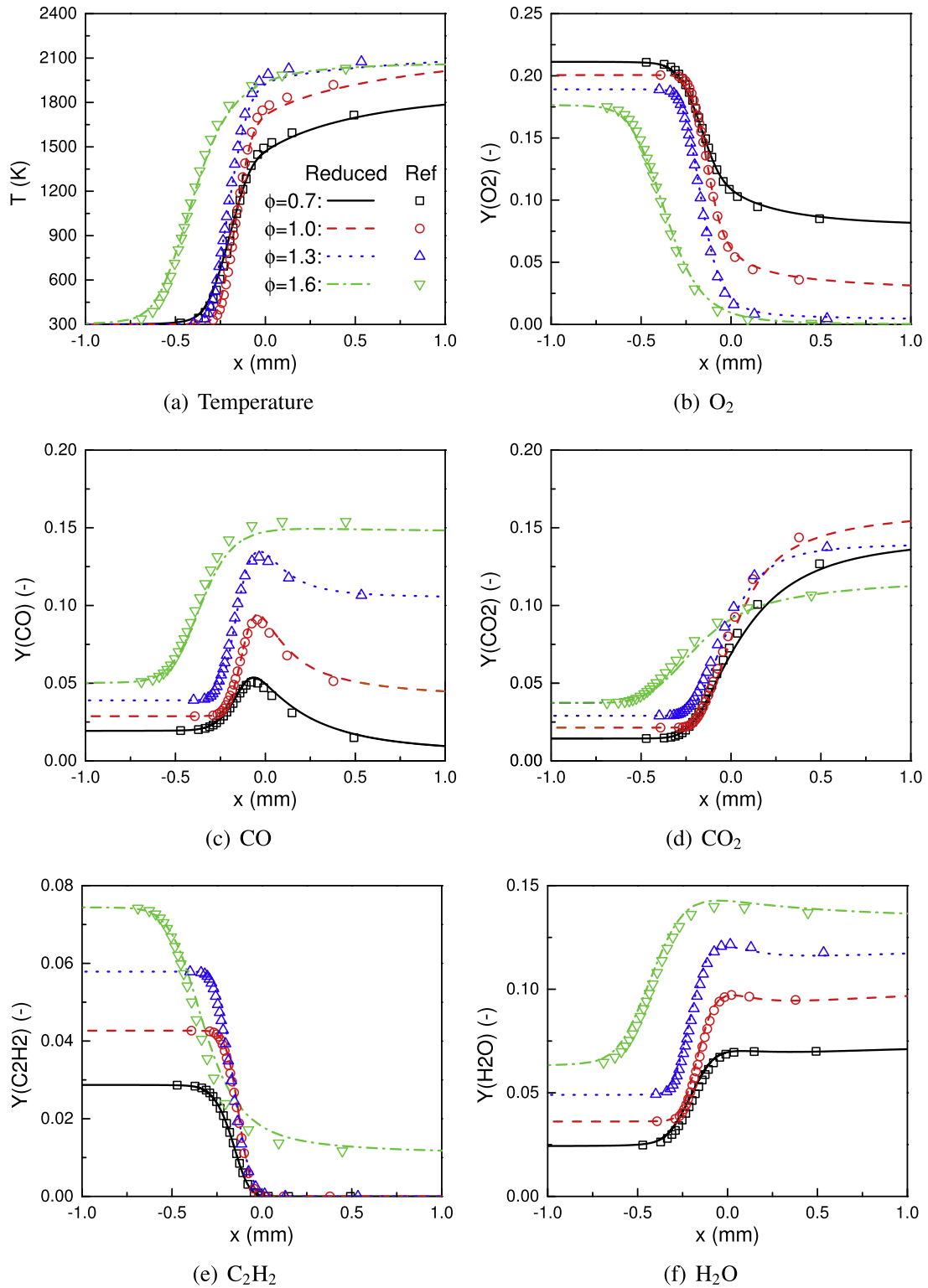
Fig. 3. Distribution of temperature and mass fractions in one-dimensional premixed flames. Black: Equivalence ratio $\phi = 0.7$. Red: 1.0. Blue: 1.3. Green: 1.6. Symbols: reference chemistry [26,42]. Lines: Reduced mechanism (DRGEP + Genetic Algorithm, Table 2). (For interpretation of the references to colour in this figure legend, the reader is referred to the web version of this article.)

$\phi^4 = 1.6$). The error measure is computed as:

$$E = \sum_{k=1}^{N_t} \left(\sum_{i=1}^{N_x} \left| \frac{\varphi_k^{\text{Ref}}(x_i; \phi^\ell) - \varphi_k(x_i; \phi^\ell)}{\varphi_k^{\text{Ref}}(x_i; \phi^\ell)} \right| \right). \tag{1}$$

During the DRGEP reduction, 6 C/H/O species and 22 Na/S/Cl species are removed with the accumulation error threshold $E = 0.16$, leading to 30 species. Then, the number of elementary reactions is further reduced down to 55 with $E = 0.18$ (Table 2 with rates parameters from [26,42].) For the hydrocarbon part, 31 elementary reactions over
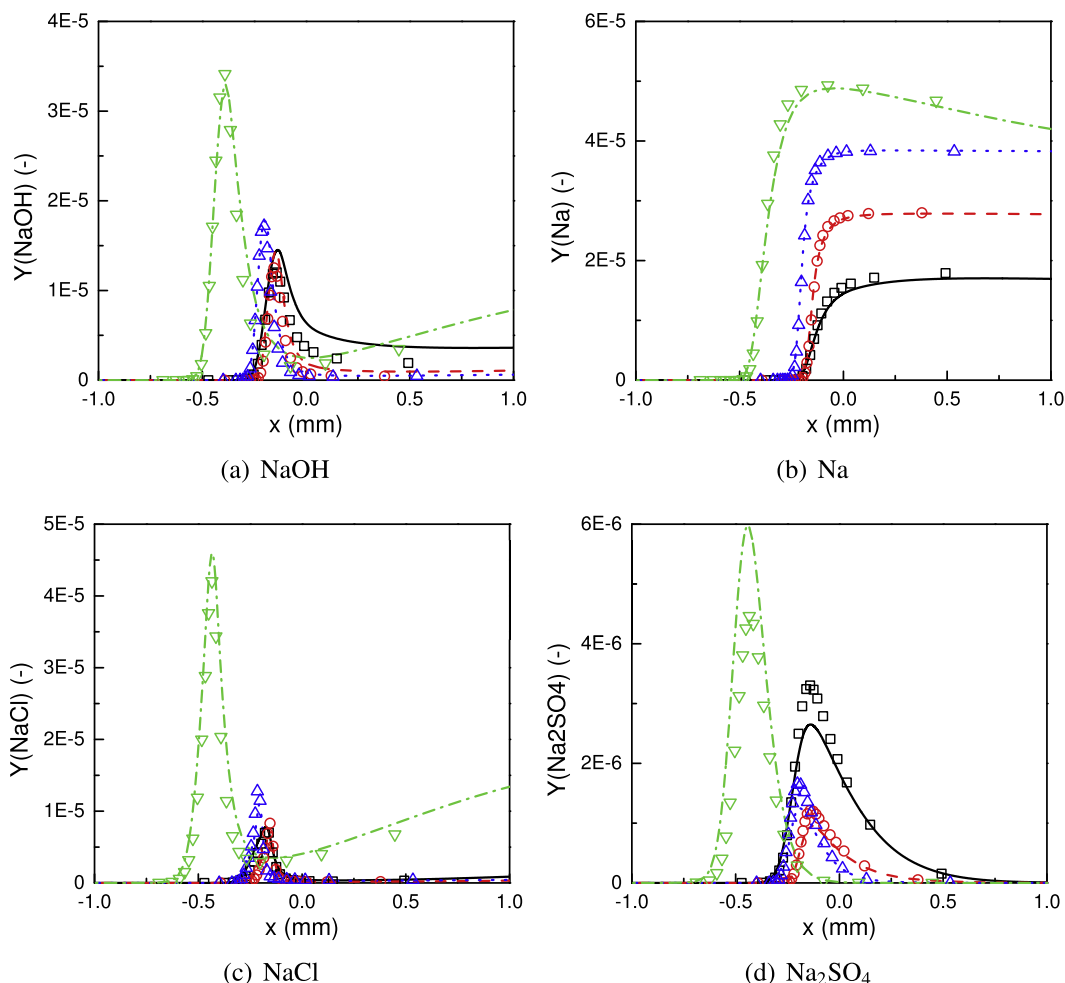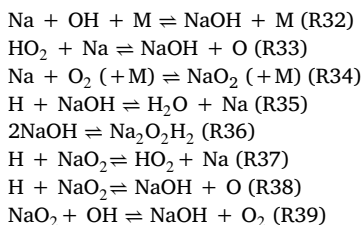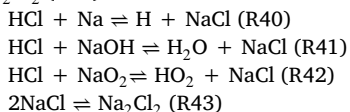
(a) NaOH

(b) Na

(c) NaCl

(d) Na$_2$SO$_4$

Fig. 4. Distribution of mass fractions in one-dimensional premixed flames. Black: Equivalence ratio $\phi = 0.7$. Red: 1.0. Blue: 1.3. Green: 1.6. Symbols: reference chemistry [26,42]. Lines: Reduced mechanism (DRGEP + Genetic Algorithm, Table 2). (For interpretation of the references to colour in this figure legend, the reader is referred to the web version of this article.)

the 104 of the skeleton mechanism [42] are kept (Table 2 from R1 to R31).
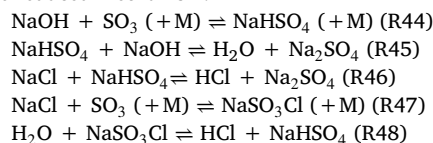
Within the Na/H/O subsystem, among the reactions ranked by DRGEP as most important for the conditions studied, 8 elementary reactions are selected over the 24 of the detailed mechanism:

$Na + OH + M \rightleftharpoons NaOH + M$ (R32)
$HO_2 + Na \rightleftharpoons NaOH + O$ (R33)
$Na + O_2 (+M) \rightleftharpoons NaO_2 (+M)$ (R34)
$H + NaOH \rightleftharpoons H_2O + Na$ (R35)
$2NaOH \rightleftharpoons Na_2O_2H_2$ (R36)
$H + NaO_2 \rightleftharpoons HO_2 + Na$ (R37)
$H + NaO_2 \rightleftharpoons NaOH + O$ (R38)
$NaO_2 + OH \rightleftharpoons NaOH + O_2$ (R39)

In this subsystem, the reactions between NaO$_2$ and the radicals H, O and OH (R37 to R39) are present along with those involving NaOH (R32, R33, R35) and its equilibrium with Na$_2$O$_2$H$_2$ (R36). The three-body reaction forming NaO$_2$ in the detailed scheme is kept in the reduced scheme (R34). In the Na/H/O/Cl subsystem, 4 elementary reactions are needed over the 9 original ones, to form NaCl from HCl and Na (R40), NaOH (R41) and NaO$_2$ (R42) and secure the equilibrium between NaCl and Na$_2$Cl$_2$ (R43):
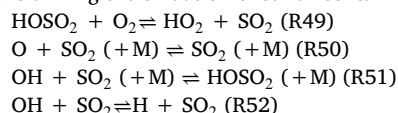
$HCl + Na \rightleftharpoons H + NaCl$ (R40)
$HCl + NaOH \rightleftharpoons H_2O + NaCl$ (R41)
$HCl + NaO_2 \rightleftharpoons HO_2 + NaCl$ (R42)
$2NaCl \rightleftharpoons Na_2Cl_2$ (R43)

Over the 17 reactions of the Na/H/O/Cl/S subsystem [26], 5 enter the reduced mechanism:

$NaOH + SO_3 (+M) \rightleftharpoons NaHSO_4 (+M)$ (R44)
$NaHSO_4 + NaOH \rightleftharpoons H_2O + Na_2SO_4$ (R45)
$NaCl + NaHSO_4 \rightleftharpoons HCl + Na_2SO_4$ (R46)
$NaCl + SO_3 (+M) \rightleftharpoons NaSO_3Cl (+M)$ (R47)
$H_2O + NaSO_3Cl \rightleftharpoons HCl + NaHSO_4$ (R48)

In this subsystem, 2 three-body reactions forming NaHSO$_4$ (R44) and NaSO$_3$Cl (R47) are kept together with the formation of NaHSO$_4$ (R48) and Na$_2$SO$_4$ (R45 and R46).

The SO$_2$/SO$_3$ interconversion subsystem includes 4 elementary reactions driving the oxidation of sulfur containing species (R49 to R52):

$HOSO_2 + O_2 \rightleftharpoons HO_2 + SO_2$ (R49)
$O + SO_2 (+M) \rightleftharpoons SO_2 (+M)$ (R50)
$OH + SO_2 (+M) \rightleftharpoons HOSO_2 (+M)$ (R51)
$OH + SO_2 \rightleftharpoons H + SO_2$ (R52)

Finally, the H/O/Cl subsystem contains only one three-body (R53) and two complementary reactions (R54 and R55) in the reduced mechanism:

$HCl + M \rightleftharpoons Cl + H + M$ (R53)
$H + HCl \rightleftharpoons Cl + H_2$ (R54)
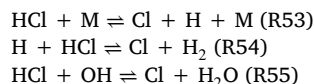$HCl + OH \rightleftharpoons Cl + H_2O$ (R55)

Fig. 1 shows the performance of this reduced mechanism. The profiles of temperature, oxygen, carbon monoxide, a major volatile component C$_2$H$_2$, and two major sodium species NaOH and Na are plotted. The

Table 2

The 30 species and 55 reactions mechanism reduced by DRGEP and kinetic rates optimized by genetic algorithm over one-dimensional premixed flames. Units are mol, s, cm^3, cal and K. The Chaperon efficiencies of the reference mechanisms [26,42] are preserved for both three-body and fall-off reactions. Electronic format available in supplementary material.

	Reaction	A	β	E_a
1	$H_2 + O \rightleftharpoons H + OH$	4.31e+04	2.79	6415
2	$HO_2 + O \rightleftharpoons O_2 + OH$	2.39e+13	0	0
3	$CH_2 + O \rightleftharpoons H + HCO$	7.34e+13	0	0
4	$CH_3 + O \rightleftharpoons CH_2O + H$	6.01e+13	0	0
5	$HCO + O \rightleftharpoons CO_2 + H$	2.92e+13	0	0
6	$C_2H_2 + O \rightleftharpoons CH_2 + CO$	8.63e+06	2.09	1893
7	$H + O_2 + M \rightleftharpoons HO_2 + M$	6.22e+18	−0.80	0
8	$H + 2O_2 \rightleftharpoons HO_2 + O_2$	2.61e+20	−1.68	0
9	$H + H_2O + O_2 \rightleftharpoons H_2O + HO_2$	5.30e+18	−0.79	0
10	$H + N_2 + O_2 \rightleftharpoons HO_2 + N_2$	2.88e+20	−1.69	0
11	$H + O_2 \rightleftharpoons O + OH$	4.83e+13	0	13957
12	$H + OH + M \rightleftharpoons H_2O + M$	5.44e+22	−2.06	0
13	$H + HO_2 \rightleftharpoons H_2 + O_2$	2.79e+13	0	1023
14	$H + HO_2 \rightleftharpoons 2OH$	6.37e+13	0	628
15	$CH_3 + H (+M) \rightleftharpoons CH_4 (+M)$	4.47e+15	−0.61	393
16	$CH_4 + H \rightleftharpoons CH_3 + H_2$	5.49e+08	1.66	11118
17	$H + HCO \rightleftharpoons CO + H_2$	3.64e+13	0	0
18	$CH_2O + H \rightleftharpoons H_2 + HCO$	5.94e+10	1.10	3237
19	$H_2 + OH \rightleftharpoons H + H_2O$	3.95e+08	1.56	3453
20	$2OH \rightleftharpoons H_2O + O$	4.17e+04	2.38	0
21	$HO_2 + OH \rightleftharpoons H_2O + O_2$	5.06e+13	0	0
22	$CH_2 + OH \rightleftharpoons CH_2O + H$	2.78e+13	0	0
23	$CH_4 + OH \rightleftharpoons CH_3 + H_2O$	9.69e+07	1.57	3032
24	$CO + OH \rightleftharpoons CO_2 + H$	3.71e+07	1.24	73
25	$HCO + OH \rightleftharpoons CO + H_2O$	1.24e+13	0	0
26	$CH_2O + OH \rightleftharpoons H_2 + HCO$	4.58e+09	1.16	0
27	$CH_3 + HO_2 \rightleftharpoons CH_4 + O_2$	1.66e+12	0	0
28	$CH_2 + O_2 \rightleftharpoons HCO + OH$	1.79e+13	0	1508
29	$H_2O + HCO \rightleftharpoons CO + H + H_2O$	8.12e+17	−0.96	17025
30	$HCO + M \rightleftharpoons CO + H + M$	6.79e+17	−0.98	17316
31	$HCO + O_2 \rightleftharpoons CO + HO_2$	2.04e+12	0	378
32	$Na + OH + M \rightleftharpoons NaOH + M$	7.13e+21	−1.72	0
33	$HO_2 + Na \rightleftharpoons NaOH + O$	1.97e+14	0	0
34	$Na + O_2 (+M) \rightleftharpoons NaO_2 (+M)$	2.72e+14	0	0
35	$H + NaOH \rightleftharpoons H_2O + Na$	1.82e+13	0	0
36	$2NaOH \rightleftharpoons Na_2O_2H_2$	1.06e+14	0	0
37	$H + NaO_2 \rightleftharpoons HO_2 + Na$	6.60e+14	0	0
38	$H + NaO_2 \rightleftharpoons NaOH + O$	1.39e+14	0	0
39	$NaO_2 + OH \rightleftharpoons NaOH + O_2$	8.54e+12	0	0
40	$HCl + Na \rightleftharpoons H + NaCl$	7.26e+14	0	10017
41	$HCl + NaOH \rightleftharpoons H_2O + NaCl$	2.06e+14	0	0
42	$HCl + NaO_2 \rightleftharpoons HO_2 + NaCl$	4.69e+14	0	0
43	$2NaCl \rightleftharpoons Na_2Cl_2$	5.41e+13	0	0
44	$NaOH + SO_3 (+M) \rightleftharpoons NaHSO_4 (+M)$	4.48e+13	0	0
45	$NaHSO_4 + NaOH \rightleftharpoons H_2O + Na_2SO_4$	1.14e+14	0	0
46	$NaCl + NaHSO_4 \rightleftharpoons HCl + Na_2SO_4$	9.48e+13	0	0
47	$NaCl + SO_3 (+M) \rightleftharpoons NaSO_3Cl (+M)$	1.21e+14	0	0
48	$H_2O + NaSO_3Cl \rightleftharpoons HCl + NaHSO_4$	2.22e+14	0	0
49	$HOSO_2 + O_2 \rightleftharpoons HO_2 + SO_3$	8.71e+11	0	637
50	$O + SO_2 (+M) \rightleftharpoons SO_3 (+M)$	3.08e+10	0	1745
51	$OH + SO_2 (+M) \rightleftharpoons HOSO_2 (+M)$	4.21e+12	0	703
52	$OH + SO_2 \rightleftharpoons H + SO_3$	4.90e+02	2.73	24365
53	$HCl + M \rightleftharpoons Cl + H + M$	1.74e+13	0	83872
54	$H + HCl \rightleftharpoons Cl + H_2$	7.75e+12	0	4320
55	$HCl + OH \rightleftharpoons Cl + H_2O$	2.51e+07	1.61	−208

Table 3

Additional $NaSO_2$-related reactions for accurate description of the very rich region in 1D diffusion flame. Units are mol, s, cm^3, cal and K.

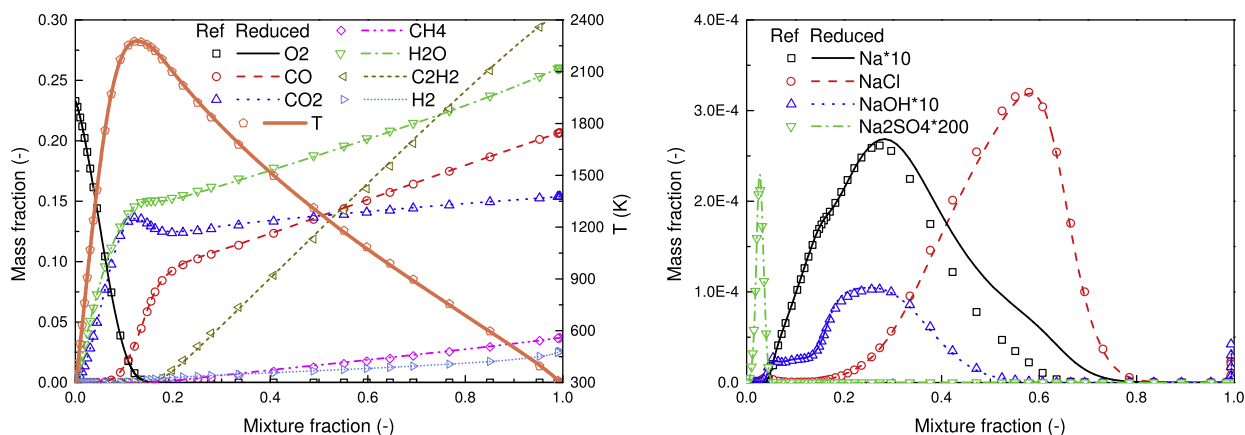|	Reaction	A	β	E_a
1	$Na + SO_2 (+M) \rightleftharpoons NaSO_2 (+M)$	1.00e+14	0	0
	Low-pressure limit:	8.80e+22	−1.50	0
2	$NaSO_2 + OH \rightleftharpoons NaOH + SO_2$	4.00e+14	0	0

ters (pre-exponential constant, temperature exponent and activation energy), with an allowed variation of ±8%. After convergence of the genetic algorithm, an optimal scheme with 30 species and 55 reactions is available (Table 2). The corresponding relative variations of the rate parameters of the elementary reactions are given in % in Fig. 2. This adjustment of the rate parameters cannot be unique, but it preserves the chemical paths and it allows for significantly improving the quality of the predictions, specifically for the rich mixture. As seen in Figs. 3 and 4, both the hydrocarbon combustion (Fig. 3) and the major sodium species $Y_{NaOH}, Y_{Na}, Y_{NaCl}$ and $Y_{Na_2SO_4}$ (Fig. 4), are now well reproduced. The reduced mechanism properly captures the fast evolution of temperature and species within the heat release zone and also the slow evolution afterwards, up to the chemical equilibrium (not shown for brevity).

2.2. Evaluation of the reduced mechanism in one-dimensional diffusion flames
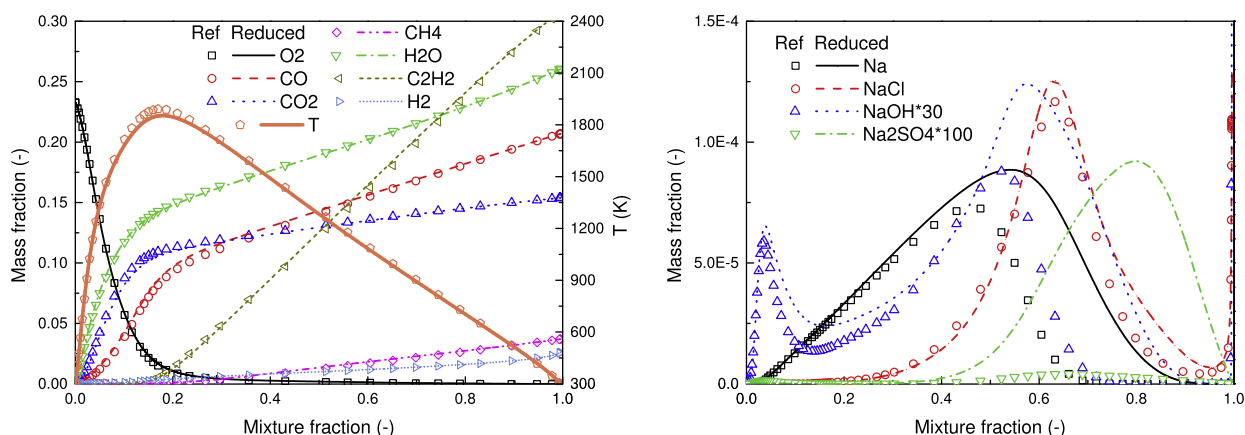
The performance of the reduced mechanism is further examined in one-dimensional counterflow diffusion flames of the volatiles (Table 1), for two representative low and high strain rate levels: 23 s^{-1} and 5052 s^{-1}. (These simulations are also performed using CANTERA [53].)

Fig. 5 shows the comparison between the detailed reference scheme [26,42] and the reduced mechanism in mixture fraction space (passive scalar with $Z = 1$ in volatiles stream and $Z = 0$ in air stream). The reduced mechanism of Table 2 returns good predictions under the low strain rate condition (23 s^{-1}) for which thermochemistry is close to chemical equilibrium. However, a departure appears on the atomic sodium on the very rich side ($Z > 0.4$) for high strain rates, although the hydrocarbon related properties, including temperature and mass fractions of O_2, CO, CO_2 and H_2O, are still well predicted for the whole range of mixture fraction (equivalence ratio). This is because the relative influence of $NaSO_2$ increases for rich mixture. Adding the two elementary reactions of Table 3 involving $NaSO_2$, the predictions on major sodium species, i.e., Na, NaCl and $NaSO_2$ are significantly improved, as shown in Fig. 6. The mass fractions of NaOH and Na_2SO_4 are still overpredicted under rich conditions. They actually feature quite small mass fractions (<3E-5), which appear to be more difficult to tackle as soon as elementary reactions are removed from the detailed chemistry. Because the volatile fuel is rapidly mixed with gases surrounding solid particles, very rich conditions ($Z > 0.4$) can seldom be observed in pulverized-coal combustion [48,57–61]. This last point is also confirmed in the DNS discussed thereafter. The two reactions of Table 3 are therefore not included in the following.

As an additional verification, one-dimensional premixed and non-premixed flames simulations have been repeated with the GRI-3.0 [62] detailed mechanism without NO$_x$ (35 chemical species and 217 elementary reactions) combined with the detailed alkali mechanism [26]. Improving the fuel oxidation chemistry from DRM22 to GRI-3.0 slightly changes the detail of ignition and also the subtle behaviour of some of the radical layers. But, it does not profoundly modify the response of the alkali part (see supplementary material), whose detailed mechanism was derived independently. Similarly, to estimate the impact of the assumptions made on alkali pollutant precursors, simulations of 1D premixed and non-premixed flames have been performed to check the performance of the reduced mechanism when NaCl is assumed to be the initial sodium compound, to confirm that the predictions of the re-

predictions of the preliminary reduced mechanism are already acceptable before optimization (second step) in the case of stoichiometric (red in Fig. 1) and fuel-lean (black in Fig. 1) mixtures. Under the fuel-rich conditions (blue and green in Fig. 1), a significant departure is observed between the reference and the reduced schemes.

This departure could be reduced by diminishing the threshold E (Eq. (1)), thus keeping more species in the mechanism. Another option to secure a minimum size mechanism while conserving accurate predictions, is to introduce a second step where a genetic algorithm is applied to optimize the rate parameters of the elementary reactions [43]. A set of $M = 48$ chromosomes is built from the chemical parame-

(a) strain rate of 23 s^{-1}

(b) strain rate of 5052 s^{-1}

Fig. 5. Species mass fractions and temperature distributions in one-dimensional diffusion flames. Symbol: reference chemistry [26,42]. Lines: reduced chemistry (Table 2).
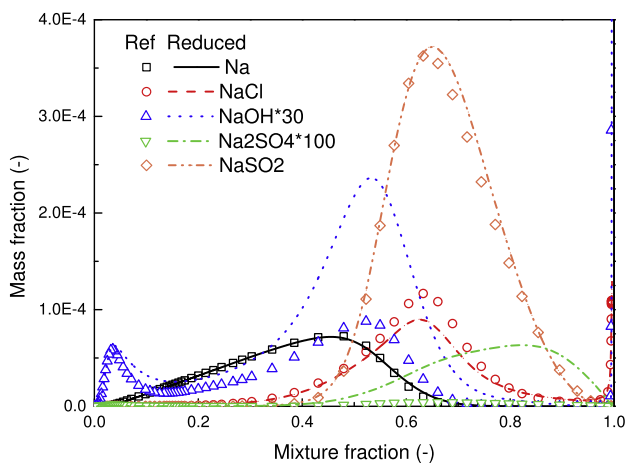

Fig. 6. Species mass fractions and temperature distributions in one-dimensional diffusion flames (strain rate 5052 s^{-1}). Symbol: reference chemistry [26,42]. Lines: reduced chemistry (Tables 2 and 3).

duced mechanism agrees well with the reference chemistry when NaOH is replaced by NaCl as the initial sodium compound (see supplementary material). The performance of the reduced mechanism has also been
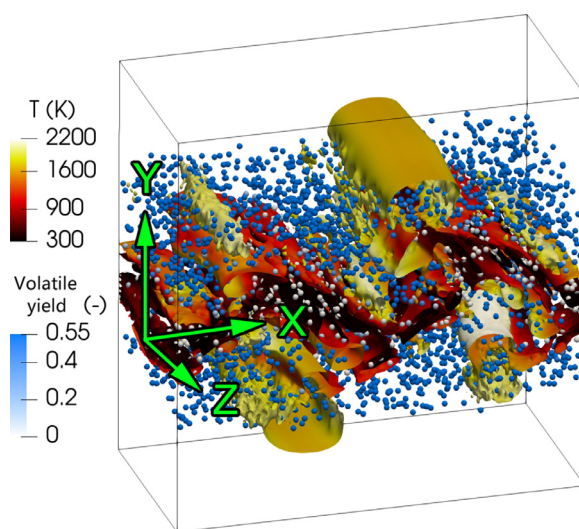
Fig. 7. Instantaneous pulverized-coal particle distribution and iso-Q criterion [63] of $Q = 10^5 \text{s}^{-2}$ colored by gas temperature. The coal particles are colored by the volatile yield, which denotes the ratio of the released volatile mass to the initial mass of a coal particle.
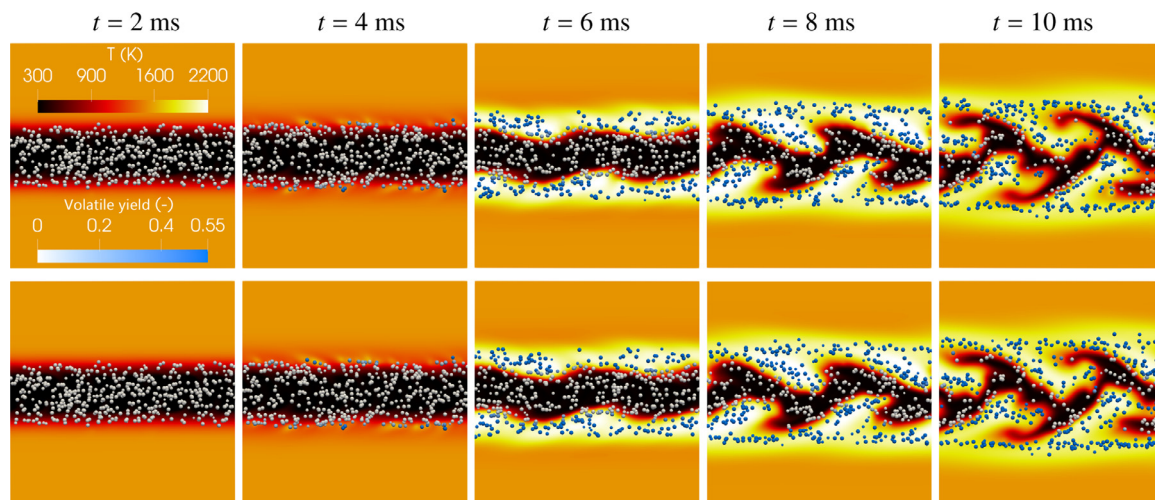
Fig. 8. Instantaneous distributions of the gas temperature and particle volatile yield at subsequent times. Transverse plane $z = 0$ and coal particles in $|z| \leqslant 100$ μm. Upper: reference mechanisms [26,42]. Lower: optimized reduced mechanism (Table 2).
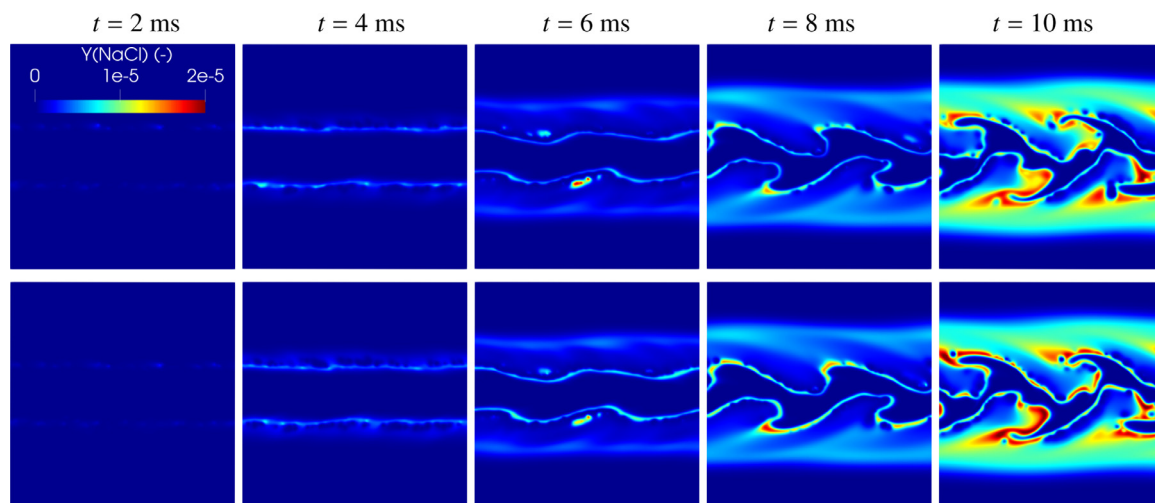
Fig. 9. Instantaneous distributions of mass fractions of NaCl at subsequent times. Transverse plane $z = 0$. Upper: reference mechanisms [26,42]. Lower: optimized reduced mechanism (Table 2).

verified when the sodium release is significantly higher or lower (see supplementary material).

Notice that the presence of NaCl in gaseous form in the fuel, in one-dimensional canonical flames, is justified by the fact that once the volatile is injected with the fuel, NaCl is produced at 300 K. First, $Na_2O_2H_2$ is produced by $2NaOH \rightleftharpoons Na_2O_2H_2$. Second, NaOH reacts with HCl in the volatile gas by $NaOH + HCl \rightleftharpoons NaCl + H_2O$, and NaCl subsequently forms Na_2Cl_2 via $2NaCl \rightleftharpoons Na_2Cl_2$. In real coal flames, the sodium species is in condensed form at low temperature. Hence, the results in the unburned region of the canonical laminar flames are questionable. This artifact will not be an issue in the simulations of 2D and 3D pulverized-coal flames discussed thereafter, as the sodium is released along with volatile and therefore at much higher temperature (see supplementary material).

The reduced mechanism is also validated against the reference chemistry in a stochastic micro-mixing problem, an approach detailed previously in [43] to produce chemical trajectories from fresh to burnt gases and cover various flow chemical compositions (see supplementary material). It might be noted that alkali species can affect NO_x emissions. However, the information of NO_x was not included in the starting reference scheme and therefore was not considered in the reduced scheme. In principle, the automated reduction procedure discussed could be re-

peated adding NO_x as target species, then appropriate pathways for NO_x would be kept.

3. Evaluation of the reduced mechanism in 3D pulverized-coal flame

3.1. DNS flow configuration

A three-dimensional DNS of a temporally evolving planar pulverized-coal jet flame with sodium emissions is now performed with the reduced mechanism (Fig. 7). The 3D coal flame operating conditions are those discussed in [30], where the detailed configurations and numerical methods can be found along with a verification of the grid resolution. The computational domain dimensions are $L_x = 25.6$ mm, $L_y = 25.6$ mm and $L_z = 12.8$ mm. A uniform mesh of $\Delta = 100$ μm is employed, which has been shown to be able to properly resolve the reaction zones [30]. Primary air (bulk velocity: 15 m/s, 300 K) laden with pulverized-coal particles is introduced for $|y| < 2.5$ mm surrounded by a hot coflow of burnt gases (3 m/s, 1559 K). Initially, the location of the coal particles follow a random uniform distribution with a particle density of 1400 kg/m^3. The pulverized-coal particles have a uniform diameter of 25 μm. The same Loy Yang brown coal is used. The coflow is the

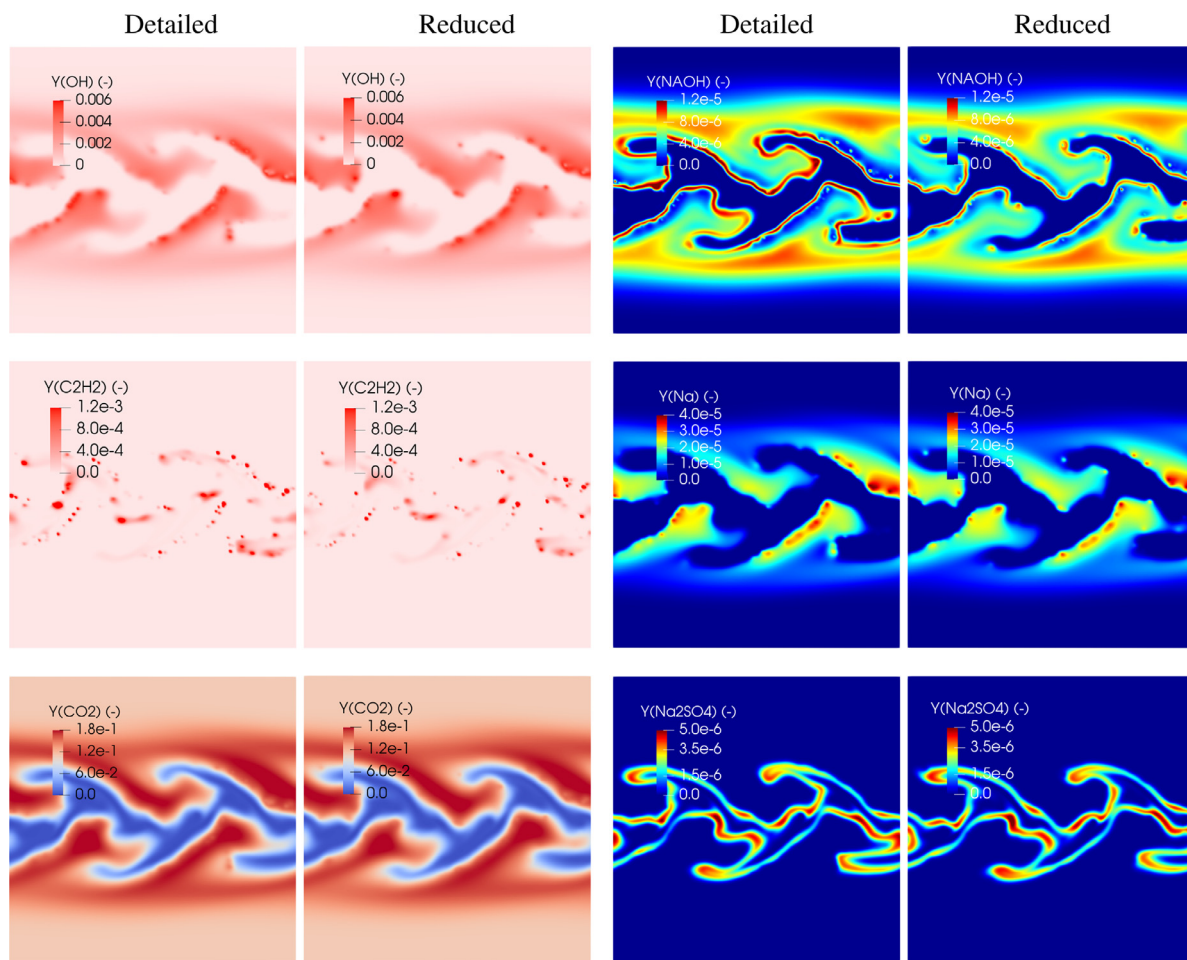**Fig. 10.** Instantaneous distributions of mass fractions of OH, NaOH, C$_2$H$_2$, Na, CO$_2$ and Na$_2$SO$_4$ at t = 10 ms. Transverse plane z = 0. Left columns: reference mechanism [26,42]. Right columns: reduced mechanism (Table 2).

burnout gas of coal volatile and air for the equivalence ratio $\phi = 0.45$ (mixture fraction $Z = 0.068$). Periodic boundary conditions are introduced in all directions. Turbulent fluctuations of 1.2 m/s (8% of the primary air velocity) are initially imposed within the shear layers between the primary jet and the coflow. The configuration of the 3D DNS mimics conditions of a pulverized-coal flame stabilized by hot burnout products such as found in real industrial furnaces. Fig. 7 is an instantaneous snapshot of the pulverized-coal flame obtained with the reduced mechanism. The turbulent flow structures are visualized by one iso-surface of the Q-criterion [63] coloured by gas temperature. The instantaneous distributions and coal particles volatile yield (ratio of the released volatile mass to the initial mass of a coal particle) are also shown.

The simulations are performed with both detailed and reduced mechanisms in the Eulerian framework for the gas phase and Lagrangian framework for the particle phase with a low-Mach number in-house code specialized in turbulent coal combustion [30,50,64–67]. The governing equations for the gas and particle phases, also accounting for radiative heat transfer, are those of Wan et al. [66]. Coal pyrolysis with sodium release, homogeneous volatile combustion and sodium reactions are simulated. Heterogeneous char reaction is not considered since its contribution has been shown to be minor in such a small-scale coal flame [48,65,68]. The porous structure of the coal particles is not explicitly included in the modeling of the solid phase. The pyrolysis rate of a pulverized-coal particle is determined by the single first-order reaction model (SFOM) [69] with its kinetic parameters, i.e., A_v (9×10^5 s^{-1}), E_v (6×10^4 J/mol) and Q_v (1.05), calibrated by the CPD model [46].

Table 4
Simulation cases with different mass fractions of HCl and SO$_2$ in the volatile compositions. The mass budget is balanced by N$_2$.

Case	NaOH	HCl	SO$_2$	Na/Cl/S molar ratio
A (baseline)	4.0E-4	6.2E-4	48.0E-4	1 / 1.7 / 7.5
B	4.0E-4	0	48.0E-4	1 / 0 / 7.5
C	4.0E-4	6.2E-4	0	1 / 1.7 / 0
D	4.0E-4	0	0	1 / 0 / 0
E	4.0E-4	3.65E-4	3.2E-4	1 / 1 / 0.5
F	4.0E-4	1.83E-4	1.6E-4	1 / 0.5 / 0.25
G	4.0E-4	0.91E-4	48.0E-4	1 / 0.25 / 7.5

The sodium vapor generated inside the porous structure of a coal particle will be transported outward by the volatile yielded and experiments have shown that the sodium release is proportional to the burnout of coal particles during the early combustion stage [19]. Thereby as in previous works [30,65,66], the sodium release rate of a pulverized-coal particle is set to be proportional to its volatile release rate. Similarly, the sulfur and chlorine release rates are also set to be proportional to the volatile release rate. The detailed composition of the volatile gas is given in Table 1.

3.2. Global flame characteristics

The performance of the reduced mechanism in the 3D pulverized-coal flame is now examined. Figs. 8 and 9 show the instantaneous dis-
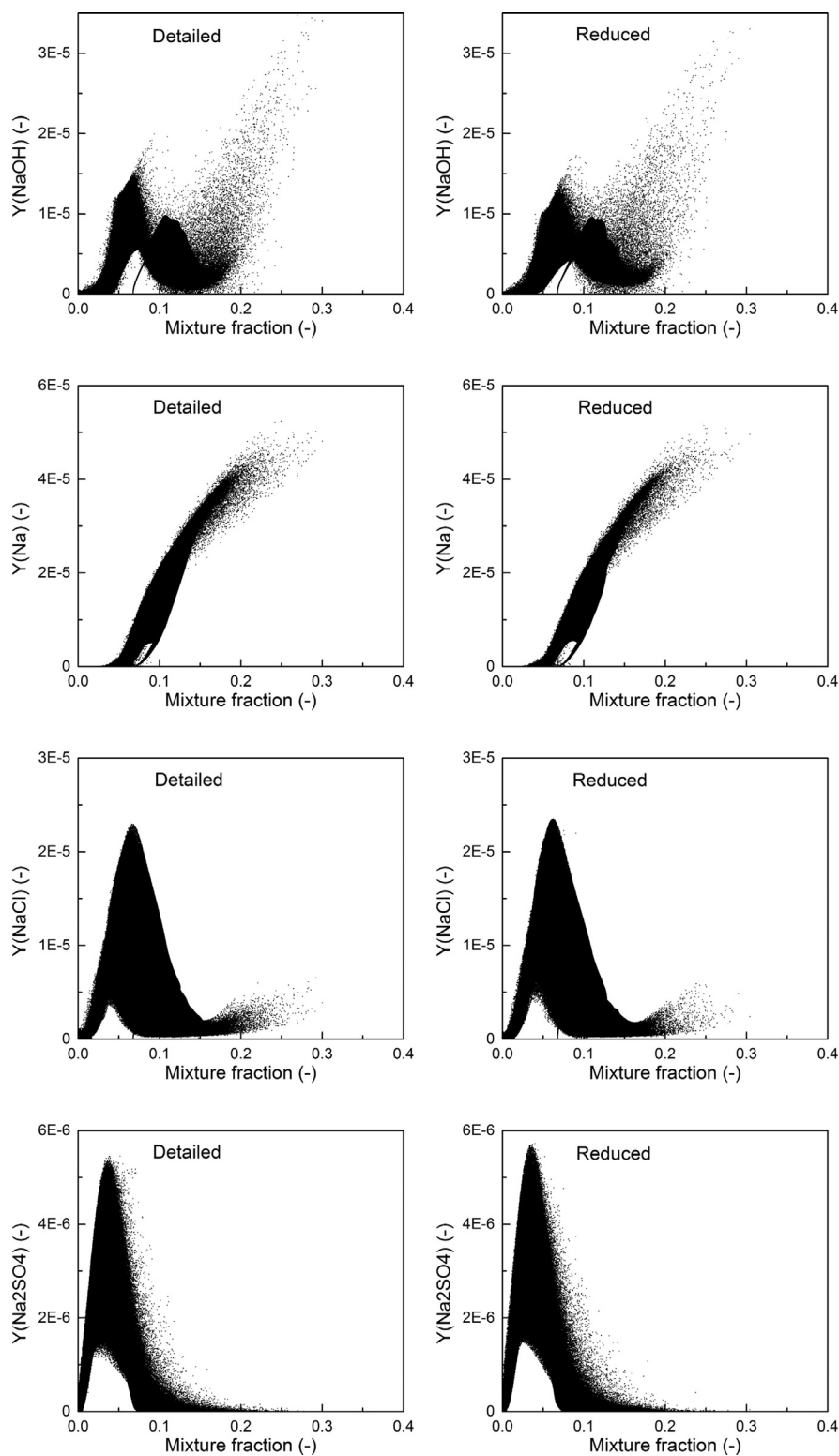
Fig. 11. Scatter plots of instantaneous mass fractions of NaOH, Na, NaCl, Na$_2$SO$_4$ against mixture fraction at t = 10 ms. Left: reference mechanism [26,42]. Right: reduced mechanism (Table 2).

tribution of the gas temperature and particle volatile yield, and NaCl mass fraction. At the early stage (t between 2 and 4 ms), coal particles in the shear layers are firstly heated up and then yield volatiles including sodium species during the pyrolysis process. At t = 6 ms, the heat release from the burning of yielded volatiles is strong enough to ignite adjacent pulverized-coal particles, leading to a continuous bright flame. The flame in turn heats up adjacent coal particles and promotes the release of volatile and sodium species, i.e., NaOH, which through sodium reactions forms the zones with a high concentration of NaCl in Fig. 9. Finally, at t = 10 ms, the flame reaction zone becomes weaker in intensity with most of the coal particles burn out, as turbulent mixing continues this reaction zone spreads within the mixing layer. The production of NaCl is then significant and high concentrations of NaCl appear. The predictions of the detailed and the reduced mechanisms are quite close to each other, except for the NaCl mass fraction at t = 10 ms, which is slightly over-predicted by the reduced mechanism.
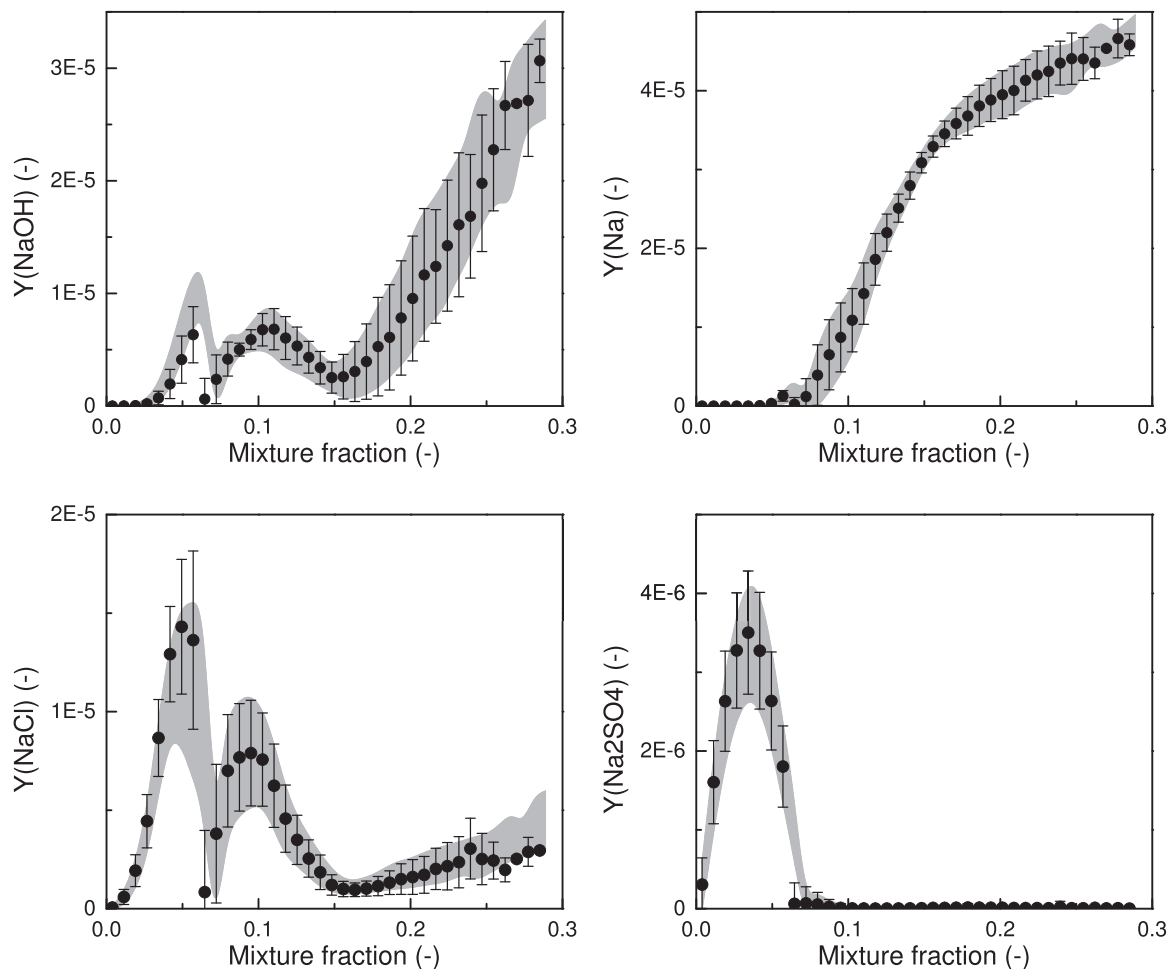
Fig. 12. Conditional mixture fraction averages at $t = 10$ ms. NaOH, Na, NaCl and Na_2SO_4. Range of the conditional mean $\pm$ fluctuation, grey bands: reference chemistry [26,42], symbols: reduced mechanism (Table 2).

Fig. 10 shows the comparisons of the DNS prediction of the detailed and reduced mechanims for OH, C_2H_2 and CO_2, and the three major sodium species, NaOH, Na and Na_2SO_4 at $t = 10$ ms. The hydrocarbon combustion part is well reproduced by the reduced mechanism. Besides C_2H_2 and CO_2, the OH radical also follows the reference mechanisms, interestingly OH was not explicitly included in the target species during the mechanism reduction and optimization procedure. Considering the sodium species, except for the mass fraction of NaOH which is slightly under-predicted in some inner shear layers, the reduced mechanism performs well.

3.3. Quantitative analysis

Fig. 11 shows the scatter plots of instantaneous mass fractions of the four major sodium species against the mixture fraction Z, as predicted by both detailed and reduced mechanisms at $t = 10$ ms. The data is obtained from every grid point of the entire 3D domain. See also Fig. 12 with $\left(\overline{Y_i | Z^*} \right)$ showing the conditional mixture fraction average and conditional root mean square (RMS), $\overline{\left[\left(\overline{Y_i | Z^*} \right) - Y_i \mid Z^* \right]^2}^{1/2}$, of species mass fractions.

The four major sodium species feature different distribution characteristics. Y_{Na} stays almost zero when $Z < 0.05$, and then increase almost linearly with Z. As previously observed in [30], the distribution

of Y_{NaOH} is more subtle. It reaches the first peak around $Z = 0.05$, to slightly drop and reach a second smaller peak around $Z = 0.1$, to drop again until the stoichiometric condition ($Z_{st} = 0.138$), and then increase for higher mixture fractions. The sharp decrease of Y_{NaOH} down to zero around $Z = 0.068$ (Fig. 12) results from the coflow stream (equivalence ratio 0.45 and $Z = 0.068$), which does not carry sodium species. The secondary decreases in the profiles of NaOH and NaCl in Fig. 12 are due to the high flame temperature around $Z_{st} = 0.138$, favouring the transformation of NaOH and NaCl to produce Na. The sulfurous sodium product Na_2SO_4 features a single-peak distribution in the fuel-lean regime ($Z < 0.138$). At a first glance, NaCl has a similar single-peak distribution (Fig. 11). However, it actually also features a double-peak distribution, which is revealed by the conditional mean of the scatter plot in Fig. 12.

This last plot (Fig 12) confirms the accuracy of the reduced mechanism. Considering that the hydrocarbon mechanism has also been reduced, the direct comparison of the prediction at one instant between reference and reduced mechanisms is actually a stringent test. To be positive, it requires accurate prediction of both hydrocarbon combustion and sodium chemistry at every time step from flow initialization, since errors accumulate.

Fig. 13 shows the time evolutions of the mean mass fractions of OH, HCl, SO_2, Z_{vol}, of major sodium species and of mean gas temperature of the pulverized-coal flame, all of which are averaged over the entire 3D computational domain. Z_{vol} is the volatile mixture fraction, a
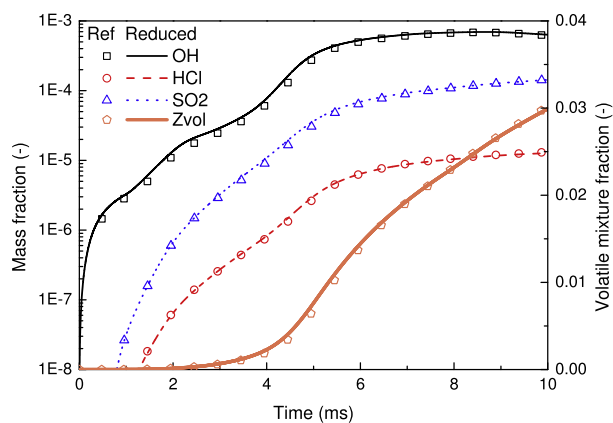
(a) Mass fractions of OH, HCl, SO$_2$ and Z_{vol}
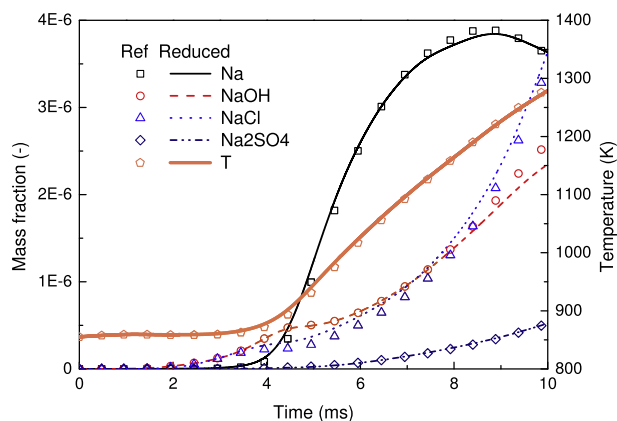
(b) Mass fractions of major sodium species and gas temperature

Fig. 13. Time evolutions of the mass fraction of species and volatiles (Z_{vol}) and gas temperature averaged over the 3D computational domain. Symbols: reference chemistry [26,42]. Lines: reduced mechanism (Table 2).

Fig. 14. Time evolution of averaged mass fractions. Black: Case A of Table 4. Blue: Case B. Red: Case C. Green: Case D. Symbols: reference chemistry [26,42]. Lines: reduced mechanism (Table 2). The range of time ∈ [15, 35] ms is zoomed in and shown on the bottom. (For interpretation of the references to colour in this figure legend, the reader is referred to the web version of this article.)

transported scalar having a source term representative of the volatile mass released from coal particles. Both Z_{vol} and T increase rapidly after $t = 4$ ms, indicating the pulverized-coal mixing layer is actively burning. The mass fractions of OH, HCl, SO$_2$ and major sodium species also start to significantly increase. Toward the end of the simulation at $t = 10$ ms, NaCl has a much higher mass fraction than Na$_2$SO$_4$. However, the concentration of HCl is an order of magnitude lower than that of SO$_2$, indicating that HCl has a much stronger ability to react with sodium species than SO$_2$. A good agreement with the reference mechanism is reached.

4. Evaluation of the reduced mechanism under different Na/Cl/S concentrations

To investigate the adaptability of the reduced mechanism when the molar ratio of Na/Cl/S in the volatile compositions varies, a parametric study is performed with different Na/Cl/S concentrations. As shown in Table 4, Case A is the original condition of the previous sections, which is used as the baseline. Cases B, C and D remove the HCl or SO$_2$, or both of them, from the volatile to explore the response of the reduced mechanism in the absence of Cl and/or S. Since the content of Cl and S in the baseline Case A is high in order to secure the combination with Na to form NaCl and Na$_2$SO$_4$, Cases E and F are set up to investigate the performance of the reduced mechanism under a lower concentration of Cl and S. Finally, Case G is employed to explore the combination of low Cl and high S mass fractions.
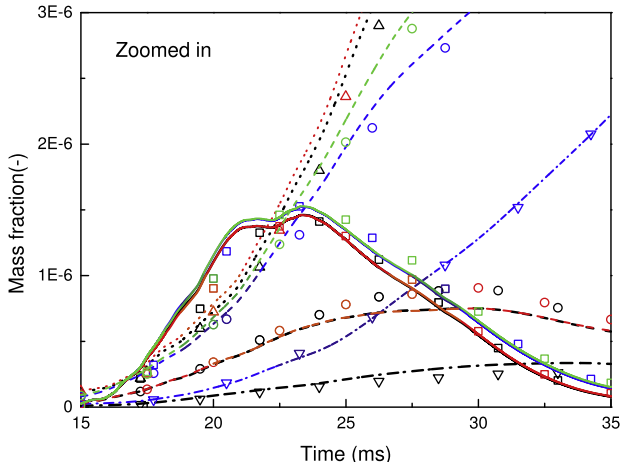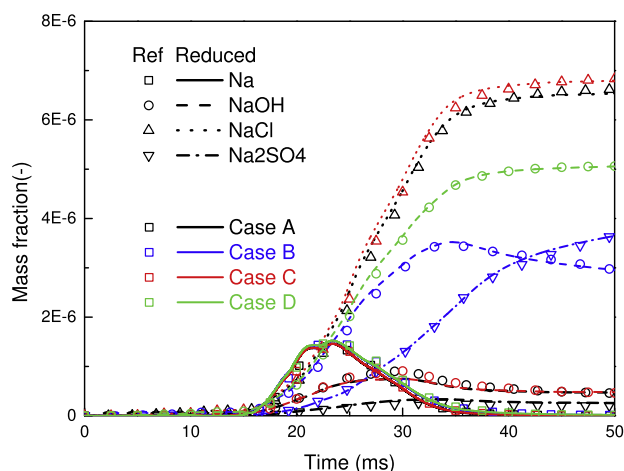
Each case of Table 4 requires two simulations with both the detailed and reduced mechanisms. It would be too expensive to perform all these DNS in 3D. Hence, 2D DNS is employed to perform the parametric study over the 14 simulation cases. The configuration of the 2D DNS is similar to the 3D one, with only some minor adjustments to secure reliable results with still a 2D domain lacking of vortex stretching in the third direction. The physical dimensions of the 2D domain are extended to both 51.2 mm in the streamwise (x) and spanwise (y) directions, with a uniform mesh resolution of 100 μm retained. The initial number of particles is also decreased down to 171. Finally, the velocity of the primary air is reduced to 10 m/s. The initial turbulent fluctuations within the shear layers are also reduced to 0.2 m/s.

Fig. 14 shows the time evolutions of the mean mass fractions of the four major sodium species among Cases A–D of Table 4, which are averaged over the entire 2D domain. The profiles of Na are similar among the four cases, reaching a peak value around $t = 23$ ms to then gradually decline to negligible concentrations at the end of the simulations. When both HCl and SO$_2$ are removed from the volatiles, NaOH becomes the main sodium product for the latter instants of the DNS ($t = 50$ ms, Case D in Fig. 14). If HCl get removed and SO$_2$ remains, NaOH is then partly transformed to Na$_2$SO$_4$, and both of them become major sodium products (Case B). If SO$_2$ is removed and HCl remains, NaOH is largely consumed by HCl to generate NaCl as the main sodium product (Case C). The sodium profiles of this last case are very similar to that of the base-
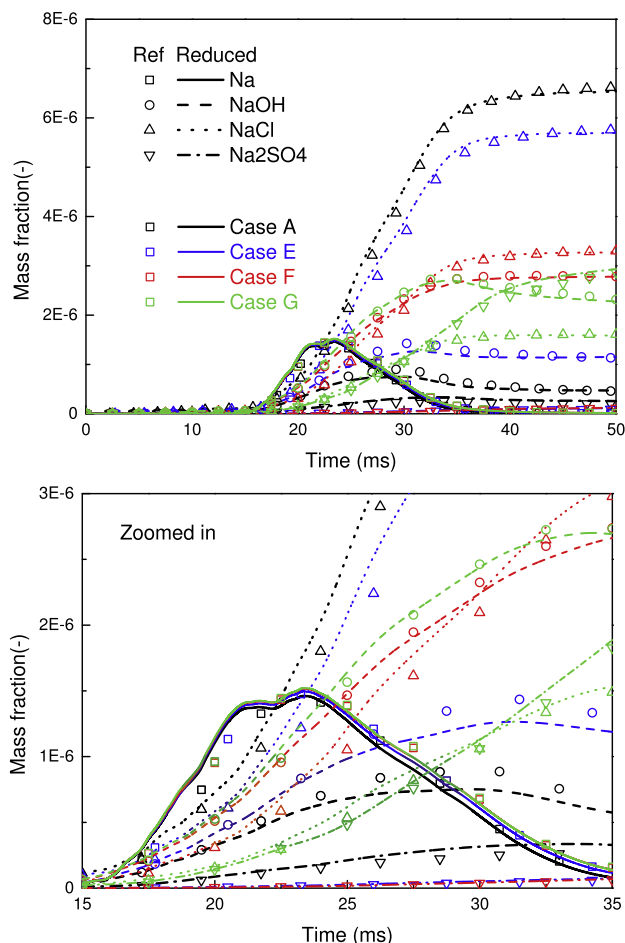
Fig. 15. Time evolution of averaged mass fractions. Black: Case A of Table 4. Blue: Case E. Red: Case F. Green: Case G. Symbols: reference chemistry [26,42]. Lines: reduced mechanism (Table 2). The range of time $\in$ [15, 35] ms is zoomed in and shown on the bottom. (For interpretation of the references to colour in this figure legend, the reader is referred to the web version of this article.)

line case (A), except that the mass fraction of NaCl in Case A is slightly lower, because a minor amount of Na_2SO_4 is formed. This finding also corroborates that SO_2 only makes a minor contribution to sodium reactions in the presence of HCl.

The average responses of Cases E–G of Table 4 on the four major sodium species are in Fig. 15. The profiles of the atomic Na of Cases E–G are also overlapped with each other and with that of the baseline Case A, which indicates that the production of Na is barely affected by the HCl and SO_2 in the volatile gases. Comparing Cases E and F, it is seen that decreasing the molar ratio of Cl/Na from 1.0 (E) to 0.5 (F), the production of NaCl is also reduced by half and NaOH appears in the products. Na_2SO_4 generated in the two cases are negligible, indicating that the molar ratio of S/Na (0.5 in Case E and 0.25 in Case F) is too low for the formation of Na_2SO_4. When the molar ratio of S/Na is increased up to 7.5 in Case G, the production of Na_2SO_4 then becomes evident.

The predictions of the reduced mechanism agree well with that of the reference one under all different Na/Cl/S configurations in the volatile. In the simulations, the particle size of 25 μm has been calibrated according to DNS requirements and it is close to the low end of a true particle-size distribution (PSD) for coal. However, the chemistry reduction is focused on the gaseous phase emitted by the coal particles and therefore the reduced mechanism can be applied to a gaseous phase emitted from coal particles with a PSD representative of a real coal burner. When the reduced mechanism is applied to other coal combustion field, the

Table 5
The gobal mechanism of sodium chemistry. Units are mol, s, cm^3, cal and K.

	Reaction	A	β	E_a
1	$O_2 + OH + SO_2 \rightleftharpoons HO_2 + SO_3$	1.36e+17	0	687
2	$H_2O + 2NaCl + SO_3 \rightleftharpoons 2HCl + Na_2SO_4$	9.86e+29	0	0
3	$HCl + Na \rightleftharpoons H + NaCl$	1.04e+15	0	11005
4	$HCl + NaOH \rightleftharpoons H_2O + NaCl$	1.40e+14	0	0
5	$2NaOH \rightleftharpoons Na_2O_2H_2$	6.08e+13	0	0
6	$2NaCl \rightleftharpoons Na_2Cl_2$	6.07e+13	0	0
7	$H + NaOH \rightleftharpoons H_2O + Na$	7.22e+13	0	0
8	$HO_2 + Na \rightleftharpoons NaOH + O$	1.28e+15	0	0

sodium part (R32-R55 of Table 2) should be directly applicable since its performance has been verified under different Na/Cl/S concentrations and also for various configurations in supplementary material. The hydrocarbon part of the reduced mechanism (R1-R31 of Table 2) may not be suitable if a significantly different type of coal is employed, because the hydrocarbon volatile compositions would be quite different from that of the present study (Table 1). In this case, the automated reduction and optimization procedure discussed in the present work can be employed to obtain a new reduced mechanism for the new type of coal. The procedure can also be extended for arbitrary combustion field in which different types of coal are mixed and fired, as in [70]. In that case, 1D premixed flames with different blending ratio of coal volatiles will also need to be considered.

5. Further reduction to a global mechanism of alkali metal emissions

Global chemical mechanisms are sometimes useful in CFD to perform numerous simulations during virtual prototyping. To build such a global mechanism 9 Na/S/Cl species have been selected according to their relative importance revealed by the DGREP approach used above. Then, the elementary reactions have been combined to derive the global mechanism given in Table 5 with rate parameters optimized using the genetic algorithm of [43] applied to one-dimensional premixed flames of equivalence ratio $\phi = 0.7$, 1.0 and 1.3 as targets.[1]

The three-dimensional DNS is repeated with the hydrocarbon part of the reduced mechanism for volatile combustion (Table 2) and the global mechanism of Table 5 for the alkali chemistry. Fig. 16 shows the conditional mixture fraction means and Fig. 17 the time evolution of their averages over the three-dimensional mixing layer. The global mechanism returns predictions which are very close to the reference detailed one. However, the predicted reaction zone thickness of Na_2SO_4 in mixture fraction space is under-estimated (Fig. 16), followed by an under-prediction of the time evolution of the mean Na_2SO_4 mass fraction (Fig. 17).

These three-dimensional simulations were run over 280 Intel Broadwell cores at 2.4 GHz. The computational costs for the three chemical mechanisms (detailed, reduced and global) are given in Fig. 18. The reduced mechanism of Table 2 saves 75% of the CPU core hours compared to the detailed one and the global mechanism provides a further 9.4% of CPU cost reduction (it should be noted that this global sodium mechanism is used along with the hydrocarbon part of the reduced mechanism).

---

[1] It was not possible to reach convergence of the genetic algorithm including also the richer condition $\phi = 1.6$ without adding more species and reaction to the global mechanism of Table 5. It is recommended to use the reduced mechanism of Table 2 if the richer condition needs to be considered, such as in the realistic combustion fields near solid-fuel burners.
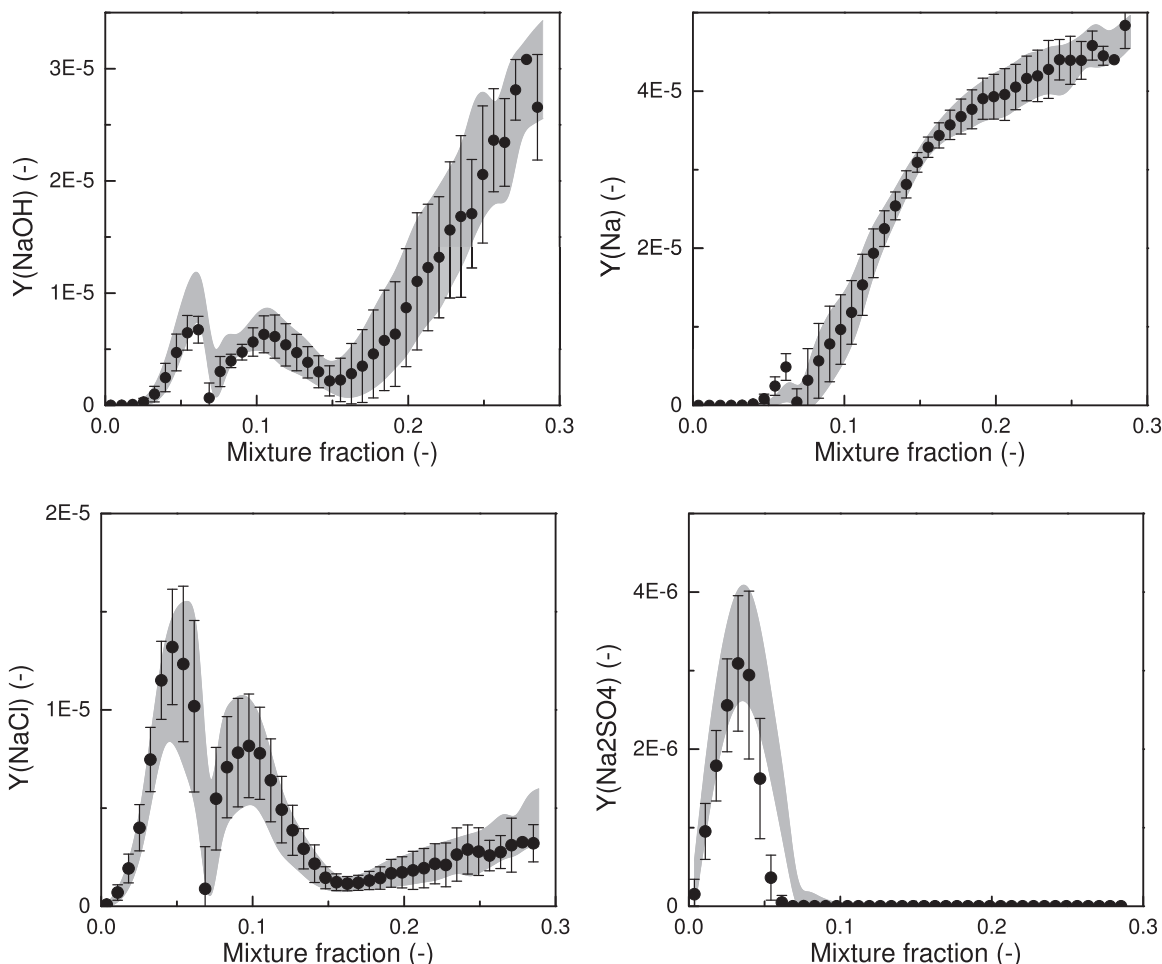
Fig. 16. Conditional mixture fraction averages at t = 10 ms. NaOH, Na, NaCl and Na$_2$SO$_4$. Range of the conditional mean $\pm$ fluctuation, grey bands: reference chemistry [26,42], symbols: global mechanism (Table 5).
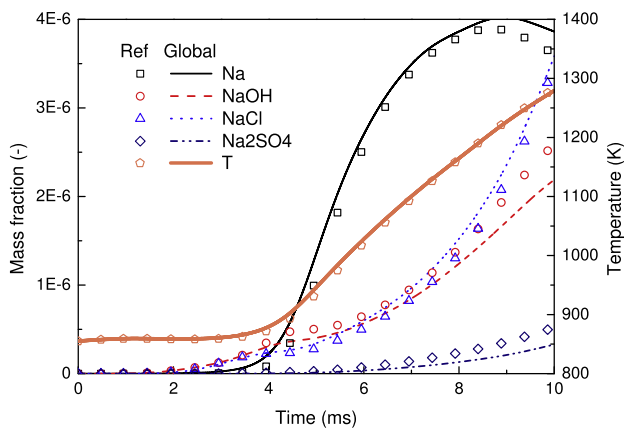

Fig. 17. Time evolutions of sodium species mass fraction and gas temperature averaged over the 3D computational domain. Symbols: reference chemistry [26,42]. Lines: global mechanism (Table 5).
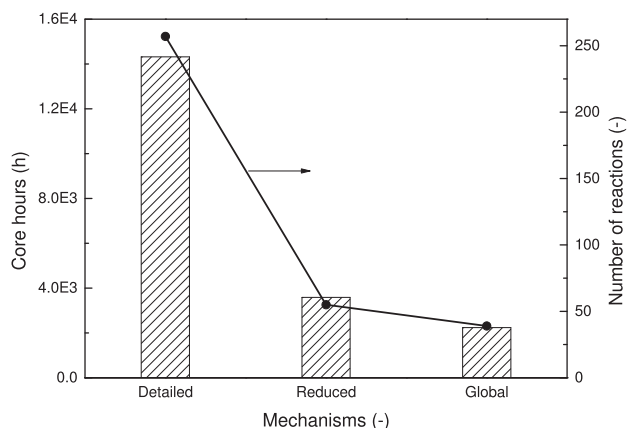

Fig. 18. CPU core hours cost of running a 3D case using the detailed, reduced and global mechanisms. The number of reactions in each mechanism is also illustrated.

6. Conclusions

An automated reduction and optimization strategy has been applied to develop reduced mechanisms for sodium chemistry during pulverized-coal combustion. The starting point is the alkali mechanism by Galborg and Marshall [26], combined with the DRM22 skeleton hy-

drocarbon oxidation mechanism by Kazakov and Frenklach [42]. The outcome of the study is a reduced mechanism for hydrocarbon combustion and sodium reactions involving 30 species and 55 elementary reactions. An additional global mechanism for sodium using only 9 Na/S/Cl species and 8 reactions is also discussed. The fuel is composed of representative volatile from coal.

These reduced mechanisms have been optimized for one-dimensional premixed flames at various equivalence ratios and validated over two more canonical flame problems, strained diffusion flames and turbulent micro-mixing. Then, three-dimensional DNS of turbulent pulverized-coal flames have been produced with the reference chemical scheme and the two reduced ones, these latter perform satisfactorily well with a CPU reduction reaching up to 84%. The reduced sodium schemes can be employed in future simulations of sodium emissions in practical solid-fuel furnaces.

The original detailed alkali mechanism [26] was validated against experimental results of the gas-phase sulfation of alkali chloride in a laminar entrained flow reactor [27]. It is used here as a reference detailed scheme for describing sodium reactions in pulverized-coal flames, i.e., not the exact conditions for which it has been developed. Hence, to consolidate this work, alkali measurement in laboratory flame would be hugely beneficial to further investigate the validity of both the detailed and reduced chemical schemes.

Declaration of Competing Interest

The authors declare that they have no known competing financial interests or personal relationships that could have appeared to influence the work reported in this paper.

Acknowledgments

Supplementary material

Supplementary material associated with this article can be found, in the online version, at 10.1016/j.jaecs.2020.100009

References

[1] Guo S, Jiang Y, Yu Z, Zhao J, Fang Y. Correlating the sodium release with coal compositions during combustion of sodium-rich coals. Fuel 2017;196:252–60. doi:10.1016/j.fuel.2017.02.004. http://www.sciencedirect.com/science/article/pii/S0016236117301497.

[2] Wang C, Zhu X, Liu X, Lv Q, Zhao L, Che D. Correlations of chemical properties of high-alkali solid fuels: A comparative study between Zhundong coal and biomass. Fuel 2018;211:629–37. doi:10.1016/j.fuel.2017.09.078. http://www.sciencedirect.com/science/article/pii/S0016236117311869.

[3] Niu Y, Tan H, Hui S. Ash-related issues during biomass combustion: Alkali-induced slagging, silicate melt-induced slagging (ash fusion), agglomeration, corrosion, ash utilization, and related countermeasures. Progress in Energy and Combustion Science 2016;52:1–61. doi:10.1016/j.pecs.2015.09.003. http://www.sciencedirect.com/science/article/pii/S0360128515300216.

[4] van Eyk PJ, Ashman PJ, Alwahabi ZT, Nathan GJ. The release of water-bound and organic sodium from Loy yang coal during the combustion of single particles in a flat flame. Combust Flame 2011;158(6):1181–92.

[5] Liu YZ, Wang ZH, Wan KD, Lv Y, Xia J, He Y, et al. In situ measurements of the release characteristics and catalytic effects of different chemical forms of sodium during combustion of Zhundong coal. Energy & Fuels 2018;32(6):6595–602. doi:10.1021/acs.energyfuels.8b00773. https://doi.org/10.1021/acs.energyfuels.8b00773.

[6] Kang Z, Ding X. Numerical analysis on combustion process and sodium transformation behavior in a 660 MW supercritical face-fired boiler purely burning high sodium content Zhundong coal. Journal of the Energy Institute 2020;93(2):450–62. doi:10.1016/j.joei.2019.07.006. http://www.sciencedirect.com/science/article/pii/S1743967119304647.

[7] Zhang Y, Xie X, Zhao J, Wei X. The alkali metal occurrence characteristics and its release and conversion during wheat straw pyrolysis. Renewable Energy 2020;151:255–62. doi:10.1016/j.renene.2019.11.013. http://www.sciencedirect.com/science/article/pii/S096014811931688X.

[8] Ji J, Cheng L, Liu Y, Wei Y, Nie L. Investigation on sodium fate for high alkali coal during circulating fluidized bed combustion. Energy & Fuels 2019;33(2):916–26. doi:10.1021/acs.energyfuels.8b03812. https://doi.org/10.1021/acs.energyfuels.8b03812.

[9] Xing H, Liu H, Zhang X, Deng H, Hu H, Yao H. Enhanced sodium adsorption capacity of kaolinite using a combined method of thermal pre-activation and intercalation-exfoliation: Alleviating the problems of slagging and fouling during the combustion of Zhundong coal. Fuel 2019;239:312–19. doi:10.1016/j.fuel.2018.11.018. http://www.sciencedirect.com/science/article/pii/S0016236118319045.

[10] Wang Y, Jin J, Liu D, Yang H, Kou X. Understanding ash deposition for Zhundong coal combustion in 330 MW utility boiler: Focusing on surface temperature effects. Fuel 2017;216:697–706. doi:10.1016/j.fuel.2017.08.112. http://www.sciencedirect.com/science/article/pii/S001623611731102X.

[11] Qi X, Song G, Song W, Yang S, Lu Q. Combustion performance and slagging characteristics during co-combustion of Zhundong coal and sludge. Journal of the Energy Institute 2018;91(3):397–410. doi:10.1016/j.joei.2017.02.002. http://www.sciencedirect.com/science/article/pii/S1743967116308303.

[12] Zhu D, Yang H, Chen Y, Li Z, Wang X, Chen H. Fouling and slagging characteristics during co-combustion of coal and biomass. BioResources 2017;12(3):6322–41. https://ojs.cnr.ncsu.edu/index.php/BioRes/article/view/BioRes_12_3_6322_Zhu_Fouling_Slagging_Characteristics_Co_combustion.

[13] Li R, Chen Q, Zhang H. Detailed investigation on sodium (Na) species release and transformation mechanism during pyrolysis and char gasification of high-Na Zhundong coal. Energy & Fuels 2017;31(6):5902–12. doi:10.1021/acs.energyfuels.7b00410. https://doi.org/10.1021/acs.energyfuels.7b00410.

[14] Yuan Y, Li S, Yao Q. Dynamic behavior of sodium release from pulverized coal combustion by phase-selective laser-induced breakdown spectroscopy. Proceedings of the Combustion Institute 2015;35(2):2339–46. https://doi.org/10.1016/j.proci.2014.07.016. http://www.sciencedirect.com/science/article/pii/S1540748914003265.

[15] Niu Y, Zhu Y, Tan H, Wang X, Hui S, Du W. Experimental study on the coexistent dual slagging in biomass-fired furnaces: Alkali- and silicate melt-induced slagging. Proceedings of the Combustion Institute 2015;35(2):2405–13. doi:10.1016/j.proci.2014.06.120. http://www.sciencedirect.com/science/article/pii/S1540748914002788.

[16] van Eyk PJ, Ashman PJ, Alwahabi ZT, Nathan GJ. Quantitative measurement of atomic sodium in the plume of a single burning coal particle. Combustion and Flame 2008;155(3):529–37. https://doi.org/10.1016/j.combustflame.2008.05.012. http://www.sciencedirect.com/science/article/pii/S0010218008001843.

[17] van Eyk PJ, Ashman PJ, Alwahabi ZT, Nathan GJ. Simultaneous measurements of the release of atomic sodium, particle diameter and particle temperature for a single burning coal particle. Proceedings of the Combustion Institute 2009;32(2):2099–106. https://doi.org/10.1016/j.proci.2008.07.038. http://www.sciencedirect.com/science/article/pii/S1540748908002927.

[18] He Y, Zhu JJ, Li B, Wang ZH, Li ZS, Aldén M, et al. In-situ measurement of sodium and potassium release during oxy-fuel combustion of lignite using laser-induced breakdown spectroscopy: effects of O_2 and CO_2 concentration. Energy & Fuels 2013;27(2):1123–30.

[19] Liu YZ, He Y, Wang ZH, Wan KD, Xia J, Liu JZ, et al. Multi-point LIBS measurement and kinetics modeling of sodium release from a burning Zhundong coal particle. Combust Flame 2018;189:77–86.

[20] Wang ZH, Liu YZ, Whiddon R, Wan KD, He Y, Xia J, et al. Measurement of atomic sodium release during pyrolysis and combustion of sodium-enriched Zhundong coal pellet. Combustion and Flame 2017;176:429–38. https://doi.org/10.1016/j.combustflame.2016.10.020. http://www.sciencedirect.com/science/article/pii/S0010218016303273.

[21] Liu YZ, Wang ZH, Xia J, Vervisch L, Wan KD, He Y, et al. Measurement and kinetics of elemental and atomic potassium release from a burning biomass pellet. Proceedings of the Combustion Institute 2019;37(3):2681–8. doi:10.1016/j.proci.2018.06.042. http://www.sciencedirect.com/science/article/pii/S1540748918302256.

[22] van Eyk PJ, Ashman PJ, Nathan GJ. Mechanism and kinetics of sodium release from brown coal char particles during combustion. Combustion and Flame 2011;158(12):2512–23. https://doi.org/10.1016/j.combustflame.2011.05.005. http://www.sciencedirect.com/science/article/pii/S0010218011001519.

[23] Fatehi H, Li ZS, Bai XS, Aldén M. Modeling of alkali metal release during biomass pyrolysis. Proceedings of the Combustion Institute 2017;36(2):2243–51. doi:10.1016/j.proci.2016.06.079. http://www.sciencedirect.com/science/article/pii/S1540748916301377.

[24] Srinivasachar S, Helble JJ, Ham DO, Domazetis G. A kinetic description of vapor phase alkali transformations in combustion systems. Progress in Energy and Combustion Science 1990;16(4):303–9. https://doi.org/10.1016/0360-1285(90)90039-6. http://www.sciencedirect.com/science/article/pii/0360128590900396.

[25] Steinberg M, Schofield K. The chemistry of sodium with sulfur in flames. Progress in Energy and Combustion Science 1990;16(4):311–17. https://doi.org/10.1016/0360-1285(90)90040-A. http://www.sciencedirect.com/science/article/pii/036012859090040A.

[26] Glarborg P, Marshall P. Mechanism and modeling of the formation of gaseous alkali sulfates. Combustion and Flame 2005;141(1–2):22–39. https://doi.org/10.1016/j.combustflame.2004.08.014. http://www.sciencedirect.com/science/article/pii/S0010218004001786.

[27] Iisa K, Lu Y, Salmenoja K. Sulfation of potassium chloride at combustion conditions. Energy & Fuels 1999;13(6):1184–90. doi:10.1021/ef990057a. https://doi.org/10.1021/ef990057a.

[28] Takuwa T, Naruse I. Emission control of sodium compounds and their formation mechanisms during coal combustion. Proc Combust Inst 2007;31(II):2863–70. doi:10.1016/j.proci.2006.07.170.

[29] Akbar S, Schnell U, Scheffknecht G. Modelling potassium release and the effect of potassium chloride on deposition mechanisms for coal and biomass-fired boilers. Combustion Theory and Modelling 2010;14(3):315–29. doi:10.1080/13647830.2010.483019. https://doi.org/10.1080/13647830.2010.483019.

[30] Wan KD, Vervisch L, Xia J, Domingo P, Wang ZH, Liu YZ, et al. Alkali metal emissions in an early-stage pulverized-coal flame: DNS analysis of reacting layers and chemistry tabulation. Proc Combust Inst 2019;37(3):2791–9.

[31] Garba MU, Ingham DB, Ma L, Porter RTJ, Pourkashnian M, Tan HZ, et al. Prediction of potassium chloride sulfation and its effect on deposition in biomass-fired boilers. Energy & Fuels 2012;26(11):6501–8. doi:10.1021/ef201681t. https://doi.org/10.1021/ef201681t.

[32] Ji J, Cheng L. CFD modeling of sodium transformation during high-alkali coal combustion in a large-scale circulating fluidized bed boiler. Fuel 2020;279:118447. doi:10.1016/j.fuel.2020.118447. http://www.sciencedirect.com/science/article/pii/S0016236120314435.

[33] Luo K, Wang H, Fan J, Yi F. Direct numerical simulation of pulverized coal combustion in a hot vitiated co-flow. Energy & Fuels 2012;26(10):6128–36. doi:10.1021/ef301253y. https://doi.org/10.1021/ef301253y.

[34] Cai R, Luo K, Watanabe H, Kurose R, Fan J. Recent advances in high-fidelity simulations of pulverized coal combustion. Advanced Powder Technology 2020;31(7):3062–79. doi:10.1016/j.apt.2020.05.001. http://www.sciencedirect.com/science/article/pii/S0921883120301928.

[35] Muto M, Yuasa K, Kurose R. Numerical simulation of soot formation in pulverized coal combustion with detailed chemical reaction mechanism. Advanced Powder Technology 2018;29(5):1119–27. doi:10.1016/j.apt.2018.02.002. http://www.sciencedirect.com/science/article/pii/S092188311830044X.

[36] Muto M, Yuasa K, Kurose R. Numerical simulation of ignition in pulverized coal combustion with detailed chemical reaction mechanism. Fuel 2017;190:136–44. doi:10.1016/j.fuel.2016.11.029. http://www.sciencedirect.com/science/article/pii/S0016236116311310.

[37] Hara T, Muto M, Kitano T, Kurose R, Komori S. Direct numerical simulation of a pulverized coal jet flame employing a global volatile matter reaction scheme based on detailed reaction mechanism. Combustion and Flame 2015;162(12):4391–407. https://doi.org/10.1016/j.combustflame.2015.07.027. http://www.sciencedirect.com/science/article/pii/S001021801500228X.

[38] Rieth M, Kempf A, Kronenburg A, Stein O. Carrier-phase DNS of pulverized coal particle ignition and volatile burning in a turbulent mixing layer. Fuel 2018;212:364–74. doi:10.1016/j.fuel.2017.09.096. http://www.sciencedirect.com/science/article/pii/S0016236117312048.

[39] Wen X, Luo K, Wang H, Luo Y, Fan J. Analysis of pulverized coal flame stabilized in a 3D laminar counterflow. Combustion and Flame 2018;189:106–25. doi:10.1016/j.combustflame.2017.10.021. http://www.sciencedirect.com/science/article/pii/S0010218017304182.

[40] Crowe CT, Sharma MP, Stock DE. The particle-source-in cell (PSI-CELL) model for gas-droplet flows. J Fluids Eng 1977;99(2):325–32.

[41] Hwang SM, Kurose R, Akamatsu F, Tsuji H, Makino H, Katsuki M. Application of optical diagnostics techniques to a laboratory-scale turbulent pulverized coal flame. Energy & fuels 2005;19(2):382–92.

[42] Kazakov A., Frenklach M. Reduced reaction sets based on GRI-mech 1.2. 1994. http://combustion.berkeley.edu/drm/.

[43] Jaouen N, Vervisch L, Domingo P, Ribert G. Automatic reduction and optimisation of chemistry for turbulent combustion modelling: Impact of the canonical problem. Combustion and Flame 2017;175:60–79. doi:10.1016/j.combustflame.2016.08.030. Special Issue in Honor of Norbert Peters.

[44] Jaouen N, Vervisch L, Domingo P. Auto-thermal reforming ATR of natural gas: An automated derivation of optimised reduced chemical schemes. Proceedings of the Combustion Institute 2017;36(3):3321–30. doi:10.1016/j.proci.2016.07.110. http://www.sciencedirect.com/science/article/pii/S1540748916303686.

[45] Aversano G, Bellemans A, Li Z, Coussement A, Gicquel O, Parente A. Application of reduced-order models based on PCA & Kriging for the development of digital twins of reacting flow applications. Comput Chem Eng 2019;121:422–41.

[46] Grant DM, Pugmire RJ, Fletcher TH, Kerstein AR. Chemical-model of coal devolatilization using percolation lattice statistics. Energy & Fuels 1989;3(2):175–86. doi:10.1021/Ef00014a011. Ac946 Times Cited:143 Cited References Count:52.

[47] Wan KD, Wang ZH, He Y, Xia J, Zhou ZJ, Zhou JH, et al. Experimental and modeling study of pyrolysis of coal, biomass and blended coal–biomass particles. Fuel 2015;139:356–64.

[48] Rieth M, Clements AG, Rabaçal M, Proch F, Stein OT, Kempf AM. Flamelet LES modeling of coal combustion with detailed devolatilization by directly coupled CPD. Proceedings of the Combustion Institute 2017;36(2):2181–9. https://doi.org/10.1016/j.proci.2016.06.077. http://www.sciencedirect.com/science/article/pii/S1540748916301353.

[49] Goshayeshi B, Sutherland JC. A comparison of various models in predicting ignition delay in single-particle coal combustion. Combustion Flame 2014;161(7):1900–10.

[50] Wan KD, Xia J, Wang ZH, Wrobel LC, Cen KF. Online-CPD-coupled large-eddy simulation of pulverized-coal pyrolysis in a hot turbulent nitrogen jet. Combust Sci Technol 2017;189(1):103–31. https://doi.org/10.1080/00102202.2016.1193498.

[51] Locci C, Vervisch L, Farcy B, Perret N. Selective non-catalytic reduction (SNCR) of nitrogen oxide emissions: a perspective from numerical modeling. Flow Turb Combust 2018;100(2):301–40.

[52] Bioche K, Ribert G, Vervisch L. Simulating upstream flame propagation in a narrow channel after wall preheating: flame analysis and chemistry reduction strategy. Combust Flame 2019;200:219–31.

[53] Goodwin D.G., Speth R.L., Moffat H.K., Weber B.W. Cantera: an object-oriented software toolkit for chemical kinetics, thermodynamics, and transport processes. https://www.cantera.org; 2018. Version 2.4.0. 10.5281/zenodo.1174508.

[54] Lu T, Law CK. A directed relation graph method for mechanism reduction. Proceedings of the Combustion Institute 2005;30(1):1333–41. doi:10.1016/j.proci.2004.08.145. http://www.sciencedirect.com/science/article/pii/S0082078404001973.

[55] Pepiot-Desjardins P, Pitsch H. An efficient error-propagation-based reduction method for large chemical kinetic mechanisms. Combustion and Flame 2008;154(1):67–81. doi:10.1016/j.combustflame.2007.10.020. http://www.sciencedirect.com/science/article/pii/S0010218007003264.

[56] Holland JH. Adaptation in natural and artificial systems: an introductory analysis with applications to biology, control and artificial intelligence. Cambridge, MA, USA: MIT Press; 1992.

[57] Stöllinger M, Naud B, Roekaerts D, Beishuizen N, Heinz S. PDF modeling and simulations of pulverized coal combustion – part 2: Application. Combustion and Flame 2013;160(2):396–410. https://doi.org/10.1016/j.combustflame.2012.10.011. http://www.sciencedirect.com/science/article/pii/S0010218012002994.

[58] Watanabe J, Yamamoto K. Flamelet model for pulverized coal combustion. Proceedings of the Combustion Institute 2015;35(2):2315–22. https://doi.org/10.1016/j.proci.2014.07.065. http://www.sciencedirect.com/science/article/pii/S1540748914003757.

[59] Rieth M, Kempf AM, Stein OT, Kronenburg A, Hasse C, Vascellari M. Evaluation of a flamelet/progress variable approach for pulverized coal combustion in a turbulent mixing layer. Proceedings of the Combustion Institute 2019;37(3):2927–34. doi:10.1016/j.proci.2018.05.150. http://www.sciencedirect.com/science/article/pii/S1540748918301561.

[60] Rieth M, Proch F, Clements A, Rabaçal M, Kempf A. Highly resolved flamelet LES of a semi-industrial scale coal furnace. Proceedings of the Combustion Institute 2017;36(3):3371–9. doi:10.1016/j.proci.2016.08.089. http://www.sciencedirect.com/science/article/pii/S1540748916304904.

[61] Wen X, Luo K, Jin H, Fan J. Numerical investigation of coal flamelet characteristics in a laminar counterflow with detailed chemistry. Fuel 2017;195:232–42. doi:10.1016/j.fuel.2017.01.068. http://www.sciencedirect.com/science/article/pii/S0016236117300789.

[62] Smith G.P., Golden D.M., Frenklach M., Moriarty N.W., Eiteneer B., Goldenberg M., et al. GRI-mech 3.0. 1999. http://combustion.berkeley.edu/gri_mech/.

[63] Hunt JCR, Wray AA, Moin P. Eddies, streams, and convergence zones in turbulent flows. In: Center for Turbulence Research Proceedings of the Summer Program; 1988. p. 193–208. CTR-S88.

[64] Wan KD, Xia J, Wang ZH, Pourkashanian M, Cen KF. Large-eddy simulation of pilot-assisted pulverized-coal combustion in a weakly turbulent jet. Flow Turbulence and Combustion 2017;99(2):531–50. doi:10.1007/s10494-017-9817-y. https://doi.org/10.1007/s10494-017-9817-y.

[65] Wan KD, Xia J, Vervisch L, Liu YZ, Wang ZH, Cen KF. Modelling alkali metal emissions in large-eddy simulation of a preheated pulverised-coal turbulent jet flame using tabulated chemistry. Combustion Theory and Modelling 2018;22(2):203–36. doi:10.1080/13647830.2017.1392043. https://doi.org/10.1080/13647830.2017.1392043.

[66] Wan KD, Wang ZH, Xia J, Vervisch L, Domingo P, Lv Y, et al. Numerical study of HCl and SO₂ impact on sodium emissions in pulverized-coal flames. Fuel 2019;250:315–26. doi:10.1016/j.fuel.2019.04.019. http://www.sciencedirect.com/science/article/pii/S0016236119305745.

[67] Wan KD, Wang ZH, Xia J, Vervisch L, Domingo P, Lv Y, et al. Numerical study of HCl and SO₂ impact on potassium emissions in pulverized-biomass combustion. Fuel Processing Technology 2019;193:19–30. doi:10.1016/j.fuproc.2019.04.032. http://www.sciencedirect.com/science/article/pii/S0378382019302826.

[68] Knappstein R, Kuenne G, Ketelheun A, Köser J, Becker L, Heuer S, et al. Devolatilization and volatiles reaction of individual coal particles in the context of FGM tabulated chemistry. Combustion and Flame 2016;169:72–84. https://doi.org/10.1016/j.combustflame.2016.04.014. http://www.sciencedirect.com/science/article/pii/S0010218016300633.

[69] Badzioch S, Hawksley PGW. Kinetics of thermal decomposition of pulverized coal particles. Ind Eng Chem Process Des Dev 1970;9(4):521–30.

[70] Muto M, Watanabe H, Kurose R. Large eddy simulation of pulverized coal combustion in multi-burner system–effect of in-furnace blending method on NO emission. Advanced Powder Technology 2019;30(12):3153–62. doi:10.1016/j.apt.2019.09.024. http://www.sciencedirect.com/science/article/pii/S092188311930336X.